The Astrophysical Journal, 996:119 (20pp), 2026 January 10 https://doi.org/10.3847/1538-4357/ae10bb

The SOFIA Massive (SOMA) Radio Survey. II. Radio Emission from High-luminosity Protostars

Francisco Sequeira-Murillo[1], Viviana Rosero[2,3,4], Joshua Marvil[3], Jonathan C. Tan[5,6], Ruben Fedriani[5,7], Yichen Zhang[6,8], Azia Robinson[9], Prasanta Gorai[10,11], Kei E. I. Tanaka[12], James M. De Buizer[13], Maria T. Beltrán[14], and Ryan D. Boyden[6]

[1] Department of Astronomy, University of Wisconsin-Madison, 475 N. Charter St., Madison, WI 53703, USA; sequeiramuri@wisc.edu
[2] Cahill Center for Astronomy and Astrophysics, MC 249-17, California Institute of Technology, Pasadena, CA 91125, USA; vrosero@caltech.edu
[3] National Radio Astronomy Observatory, 1003 López ville Rd., Socorro, NM 87801, USA
[4] Space Science Institute, 4750 Walnut Street, Suite 205, Boulder, CO 80301, USA
[5] Department of Space, Earth & Environment, Chalmers University of Technology, 412 93 Gothenburg, Sweden
[6] Department of Astronomy, University of Virginia, Charlottesville, VA 22904, USA
[7] Instituto de Astrofísica de Andalucía, CSIC, Glorieta de la Astronomía s/n, 18008 Granada, Spain
[8] State Key Laboratory of Dark Matter Physics, School of Physics and Astronomy, Shanghai Jiao Tong University, Shanghai 200240, People's Republic of China
[9] Department of Physics and Astronomy, Agnes Scott College, 141 E. College Ave. Decatur, GA 30030, USA
[10] Rosseland Centre for Solar Physics, University of Oslo, PO Box 1029 Blindern, 0315, Oslo, Norway
[11] Institute of Theoretical Astrophysics, University of Oslo, PO Box 1029 Blindern, 0315, Oslo, Norway
[12] Department of Earth and Planetary Sciences, Institute of Science Tokyo, Meguro, Tokyo 152-8551, Japan
[13] Carl Sagan Center for Research, SETI Institute, Mountain View, CA, USA
[14] INAF-Osservatorio Astrofisico di Arcetri, Largo E. Fermi 5, I-50125 Firenze, Italy
Received 2025 July 21; revised 2025 October 6; accepted 2025 October 6; published 2026 January 9

Abstract

We present centimeter continuum observations of seven high-luminosity massive protostars and their surrounding sources in regions with multiple targets, as part of the SOFIA Massive (SOMA) Star Formation Survey. With data from the Very Large Array and the Australia Telescope Compact Array, we analyze the spectral index, morphology, and multiplicity of the detected radio sources. The high-sensitivity, high-resolution observations allow us to resolve many sources; 65% of the reported sources are resolved at least within the synthesized beam. We report 15 new detections, 13 of which are entirely new, and 2 have counterparts at other wavelengths but are detected here for the first time at radio frequencies. We use the observations to build radio spectral energy distributions to calculate spectral indices. With radio morphologies and the spectral indices, we give assessments on the nature of the sources, highlighting six sources that display a radio jetlike morphology and a spectral index consistent with ionized jets. Combining with the SOMA Radio I sample, we present the radio–bolometric luminosity relation, especially probing the regime from $L_{\rm bol} \sim 10^4$ to $10^6 L_\odot$. Here, we find a steep rise in radio luminosity, which is expected by models that transition from shock ionization to photoionization.

Unified Astronomy Thesaurus concepts: Radio jets (1347); Star formation (1569); Radio interferometry (1346); Stellar jets (1607); Interstellar medium (847)

1. Introduction

Massive stars impact many processes in astrophysics, yet crucial aspects of their formation remain uncertain due to observational difficulties given by their relative rarity and large distances (typically >1 kpc), crowded environments, and high extinctions (J. C. Tan et al. 2014). Various theories have been proposed to explain the formation of massive stars, but there is no general consensus on the basic nature of the formation mechanism. Theories range from the turbulent core accretion (TCA) model (C. F. McKee & J. C. Tan 2003) to competitive accretion (e.g., I. A. Bonnell et al. 2001; P. Wang et al. 2010; M. Y. Grudić et al. 2022) to protostellar collisions (I. A. Bonnell et al. 1998).

High-sensitivity centimeter continuum observations can provide a valuable understanding of the earliest and most obscured phases of high-mass star formation. K. E. I. Tanaka et al. (2016; hereafter TTZ16) developed models to predict the ionization structures and centimeter continuum emission properties using initial parameters from a physical model based on TCA, including infall envelope, disk and outflow properties and their predicted thermal spectral energy distribution (SED; Y. Zhang & J. C. Tan 2011, 2018; Y. Zhang et al. 2013, 2014). V. Rosero et al. (2016, 2019a) demonstrated that many centimeter continuum sources have morphologies and parameters indicative of ionized jets, which is consistent with the results from the free–free emission models developed by TTZ16. This makes radio continuum emission highly relevant for constraining the ionizing luminosity of a protostar and helping to develop and test theoretical models for the evolutionary sequence of massive star formation.

In order to carry out such tests, one needs a sample of massive protostars that ideally spans a range of core properties, evolutionary stages, and environments. The SOFIA Massive (SOMA) Star Formation Survey (PI: J. Tan) was developed with such goals in mind. It aims to characterize a sample of $\geqslant$50 high and intermediate-mass protostars over a range of initial core masses, evolutionary stages, and environments using SOFIA-FORCAST $\sim$ 10–40 μm data. In Paper I of the survey (J. M. De Buizer et al. 2017; hereafter SOMA I), the first eight sources were presented, which were mostly massive

Table 1
SOMA Sources: Radio Continuum Data

Region	Frequency Band (GHz)	R.A (J2000)	Decl. (J2000)	Beam Size ($'' \times ''$, degree)	rms (μJy beam^{-1})	d [a] (kpc)	$L_{\rm bol,\ iso}$ [b] ($L_\odot$)	$L_{\rm bol}$ [b] ($L_\odot$)
G45.12+0.13[c]	4.0–8.0	19 13 27.86	+10 53 36.6	0.26 × 0.25, −45.5	35	7.40	$4.4^{+4.4}_{-2.2} \times 10^5$	$8.0^{+6.5}_{-3.6} \times 10^5$
	18.0–26.0	...	...	0.33 × 0.25, −53.2	120	⋯	⋯	⋯
G309.92+0.48[d]	5.5–9.0	13 50 41.85	−61 35 10.4	1.09 × 0.89, +12.3	560	5.50	$3.1^{+0.8}_{-0.6} \times 10^5$	$6.6^{+4.8}_{-2.8} \times 10^5$
	17.0–22.8	⋯	⋯	0.83 × 0.52, −11.1	820	⋯	⋯	⋯
G35.58-0.03[c]	4.0–8.0	18 56 22.56	+02 20 27.7	0.32 × 0.27, +64.7	8	10.2	$2.4^{+0.3}_{-0.3} \times 10^5$	$4.3^{+2.9}_{-1.7} \times 10^5$
	18.0–26.0	⋯	⋯	0.30 × 0.29, +73.5	90	⋯	⋯	⋯
IRAS 16562-3959[d,e]	5.0–9.0	16 59 41 63	−40 03 43.6	2.49 × 1.36, −4.13	21	1.70	$4.9.0^{+1.9}_{-1.3} \times 10^4$	$2.2^{+2.5}_{-1.2} \times 10^5$
	17.0–19.0	⋯	⋯	0.78 × 0.39, +2.87	28	⋯	⋯	⋯
G305.20+0.21[d]	5.5–9.0	13 11 10.49	−62 34 38.8	0.97 × 0.82, +86.5	70	4.10	$6.2^{+1.7}_{-1.4} \times 10^4$	$2.1^{+2.0}_{-1.0} \times 10^5$
	17.0–22.8	⋯	⋯	0.61 × 0.40, −6.59	70	⋯	⋯	⋯
G49.27-0.34[c]	4.0–8.0	19 23 06.61	+14 20 12.0	0.29 × 0.26, +64.3	6	5.55	$1.4^{+2.8}_{-0.9} \times 10^5$	$1.0^{+0.5}_{-0.3} \times 10^5$
	18.0–26.0	⋯	⋯	0.33 × 0.26, −62.2	9	⋯	⋯	⋯
G339.88-1.26[d,f]	5.5–9.0	16 52 04.67	−46 08 34.2	2.38 × 1.44, −16.3	25	2.10	$3.8^{+1.6}_{-1.1} \times 10^4$	$9.1^{+16.0}_{-5.8} \times 10^4$
	17.0–22.8	⋯	⋯	0.90 × 0.34, −1.09	75	⋯	⋯	⋯

Notes. Units of R.A. are hours, minutes, and seconds. Units of decl. are degrees, arcminutes, and arcseconds.
[a] References cited in SOMA II.
[b] Average and dispersion of the bolometric luminosities of the good models from SOMA V. These values and other intrinsic properties are reported in Table C1.
[c] Images from the VLA.
[d] Images from ATCA.
[e] Images obtained from Andrés Guzmán (via public personal archive). Observations reported in A. E. Guzmán et al. (2016).
[f] Images obtained from Simon Purser (via private communication). Observations reported in S. J. D. Purser et al. (2016).

protostars. In Paper II (M. Liu et al. 2019; hereafter SOMA II), seven high-luminosity sources were presented, representing some of the most massive protostars in the survey. In Paper III (M. Liu et al. 2020; hereafter SOMA III), 14 intermediate-mass sources were presented. In Paper IV (R. Fedriani et al. 2023; hereafter SOMA IV), 11 isolated sources, based on the 37 μm imaging, were presented. In Paper V, Z. Telkamp et al. (2025; hereafter SOMA V), seven regions of relatively clustered massive star formation were studied.

The SOMA Radio Survey was developed with the goal of obtaining centimeter radio continuum observations of the SOMA sample, i.e., to have more comprehensive wavelength coverage of "extended spectral energy distributions" (E-SEDs) that constrains ionized gas properties and thus help break degeneracies that arise in infrared-only SED inferred properties from the standard SOMA analysis based on the Y. Zhang & J. C. Tan (2018; hereafter ZT18) TCA model grid. In SOMA Radio Paper I (V. Rosero et al. 2019b; hereafter SOMA Radio I), the first eight sources of SOMA I were observed with the Karl G. Jansky Very Large Array (VLA) and the centimeter continuum data presented and analyzed, including comparison to the TTZ16 models for free–free emission.

In this paper, the second in the radio series, we present ATCA and VLA data of the seven high-luminosity regions of SOMA II, containing a total of nine sources, i.e., after adding IRAS 16562–3959 N and G305.20+0.21 A, which were reported and analyzed in SOMA III.

Our approach follows the general methods developed in SOMA Radio I to analyze the data. In particular, we construct radio SEDs by reducing the centimeter continuum observations, measuring the fluxes from the images, and analyzing the morphology and multiplicity of each region. We define multiplicity in a region when it contains two or more 5σ detections that are not necessarily associated with each other. We note that due to improvements in the infrared SED analysis, including a new algorithm to calculate the optimal aperture size in an unbiased and reproducible way for extended sources, updates in the SED fitting tool and revised methods assessing uncertainties in background subtracted fluxes, we use the infrared inferred results (e.g., bolometric luminosities) from SOMA V, rather than the results from SOMA II.

The paper is organized as follows: Methodology and information regarding the observations are presented in Section 2. The observational results for each source are presented in Section 3, while the analysis and discussion of the sample are presented in Section 4. A summary and our conclusions are presented in Section 5.

2. Methods

The SOMA Star Formation Survey sample is defined by SOFIA-FORCAST observations (i.e., from ∼7 to 40 μm). The sample we analyze in this paper is part of the protostars presented by SOMA II, as well as sources IRAS 16562–3959 N and G305.20+0.21A that were reported in SOMA III, as an addendum to the sources in the SOMA II regions. Thus, a total of nine protostars in seven target regions will be analyzed: G45.12+0.13, G309.92+0.48, G35.58–0.03, IRAS 16562–3959, IRAS 16562–3959 N, G305.20+0.21, G305.20+0.21 A, G49.27–0.34, and G339.88–1.26. The radio observations presented here are our own VLA observations for regions G45.12+0.13, G35.58–0.03, and G49.27–0.34. For G305.20+0.21 and G309.92+0.48, we present our own ATCA observations, and for regions IRAS 16562–3959 and G339.88–1.26, we used ATCA observations reported by A. E. Guzmán et al. (2016) and S. J. D. Purser et al. (2016), respectively.

The data analyzed in this work are summarized in Table 1. Column (1) gives the region name; columns (2), (3), and (4) provide the band frequency, R.A., and decl., respectively; columns (5) and (6) give the synthesized beam size and position angle, and the rms of the resulting images. The distance, as adopted by SOMA II, as well as the bolometric

Table 2
VLA Calibrators

Calibrator	Astrometry Precision[a]	Source Calibrated	Band
J1922+1530	A	G45.12+0.13	*C*
J1924+1540	A	G45.12+0.13	*K*
J1824+1044	A	G35.58-0.03	*C*
J1851+0035	C	G35.58-0.03	*K*
J1922+1530	A	G49.27-0.34	*C*
J1925+2100	A	G49.27-0.34	*K*

Note.
[a] Astrometric precisions of *A*, *B*, and *C* correspond to positional accuracies of $<0\farcs002$, $0\farcs002$–$0\farcs01$ and $0\farcs01$–$0\farcs15$, respectively.

Table 3
Observation Times for Sources Observed Using the VLA

Source	Band	Target Source[a] (minutes)	Phase Calibrator[a] (minutes)	Total Integration (minutes)
G45.12+0.13	*C*	8.4	0.45	42
	K	1.2	0.54	23
G35.58-0.03	*C*	8.2	0.52	41
	K	2.5	0.62	23
G49.27-0.34	*C*	8.6	0.65	43
	K	2.3	0.51	20

Note.
[a] Alternating time from the source to the calibrator.

luminosities and the isotropic bolometric luminosity evaluated by SOMA V, are shown in columns (7), (8), and (9), respectively. A list of phase calibrators used in the VLA observations at 1.3 and 6 cm is given in Table 2.

2.1. VLA Data

2.1.1. The 6 cm Data

The 6 cm (*C* band) observations were carried out in the A configuration, providing angular resolutions $\sim0\farcs3$ and a largest angular scale (LAS or $\theta_{\rm LAS}$) of $8\farcs9$. The project code for the observations of regions G35.58-0.03 and G49.27-0.34 is 18A-294 (PI: V. Rosero), and for region G45.12+0.13 is 19A-216 (PI: V. Rosero). The data consist of two ∼2 GHz wide basebands (3 bit samplers) centered at 5.03 and 6.98 GHz. The data were recorded in 30 unique spectral windows (SPWs), each comprised of 64 channels and each channel being 2 MHz wide, resulting in a total bandwidth of 3842 MHz (before "flagging"). Source 3C48 was used as flux density and bandpass calibrator for regions G35.58-0.03 and G49.27-0.34, and 3C286 for region G45.12+0.13.

The data were processed using NRAO's Common Astronomy Software Applications (CASA) package, and we use calibrated data from the VLA Calibration Pipeline version 41154 (Pipeline-CASA51-P2-B) for regions G35.58-0.03 and G49.27-0.34, and the VLA Calibration Pipeline version 42270 (Pipeline-CASA54-P2-B) for region G45.12+0.13. The images were made using the tclean task and Briggs Robust = 0.5 weighting (D. S. Briggs 1995). Imaging of regions G35.58-0.03 and G45.12+0.13 also included one round of phase-only self calibration using solution intervals ranging from 30 s to 60 s, depending on frequency.

For all the regions, we made two images, each of a ∼2 GHz baseband composed of 15 SPWs, and also a combined image using data from both basebands with a total of 30 SPWs. All maps were primary beam-corrected. Columns (5) and (6) of Table 1 list the synthesized beam (size and position angle) and the rms of the combined images.

Table 3 shows approximations of the observation times for each region at both 6 and 1.3 cm bands. All the observations were made alternating between the target source and the phase calibrator. Columns (3) and (4) show these alternating times, and column (5) shows the total on-source integration time for each observation.

2.1.2. The 1.3 cm Data

The 1.3 cm (*K* band) observations were made in the B configuration, providing angular resolutions $\sim0\farcs4$ and an LAS (or $\theta_{\rm LAS}$) of $7\farcs9$ The project code for all observations in this band is 19A-216 (PI: V. Rosero). The data consist of two ∼4 GHz wide basebands (3 bit samplers) centered at 20.4 and 24.4 GHz. The data were recorded in 60 unique SPWs, comprised of 64 channels and each channel being 2 MHz wide, resulting in a total bandwidth of 7680 MHz, before "flagging." Source 3C286 was used as flux density and bandpass calibrator. The data reduction was done in the same manner as that for the *C*-band observations, using the VLA Calibration Pipeline version 42270 (Pipeline-CASA54-P2-B) for all the regions.

The images were made using the tclean task and Briggs Robust = 0.5 weighting. We made two images, each of a ∼4 GHz baseband composed of 30 SPWs, and also a combined image using data from both basebands with a total of 60 SPWs. All maps were primary beam-corrected. Columns (5) and (6) of Table 1 show the synthesized beam (size and position angle) and the rms of the combined images.

2.2. ATCA Data

For regions G309.92+0.48 and G305.20+0.21, we used our own ATCA observations; meanwhile, for regions IRAS 16562-3959 and G339.88-1.26, we used ATCA observations reported by A. E. Guzmán et al. (2016) and S. J. D. Purser et al. (2016).

In the following, we describe our new ATCA observations. The project code of the observations for the regions G309.92+0.48 and G305.20+0.21 is C3396 (PI: V. Rosero). These observations were made using ATCA in the 6A and 6B configurations in 2020 October. Observations were made at four frequencies: 5.5, 9.0, 17.0, and 22.8 GHz, each with a bandwidth of 2048 MHz (XX, YY, XY, and YX polarizations) that was split into channels of width 1 MHz.

Individual scan times on flux and phase calibrators were 5 minutes and 90 s, respectively, and on target sources were between 3 and 45 minutes, depending on atmospheric conditions and observing frequencies. The average total integration time on each science target was 75 minutes. The bandpass and flux density were calibrated with source B1934–638 using the Stevens–Reynolds 2016 model (B. Partridge et al. 2016). The ATCA data were calibrated in CASA following standard interferometric procedures for flagging, flux-density transfer, and phase referencing. Imaging of region G305.20+0.21 also included one round of phase-only self calibration using solution intervals ranging from 30 s to 60 s, depending on frequency.

For the two regions observed with project code C3396, we made four images centered around the four frequencies previously described. However, similarly to the VLA observations, we also made two additional images with the combined

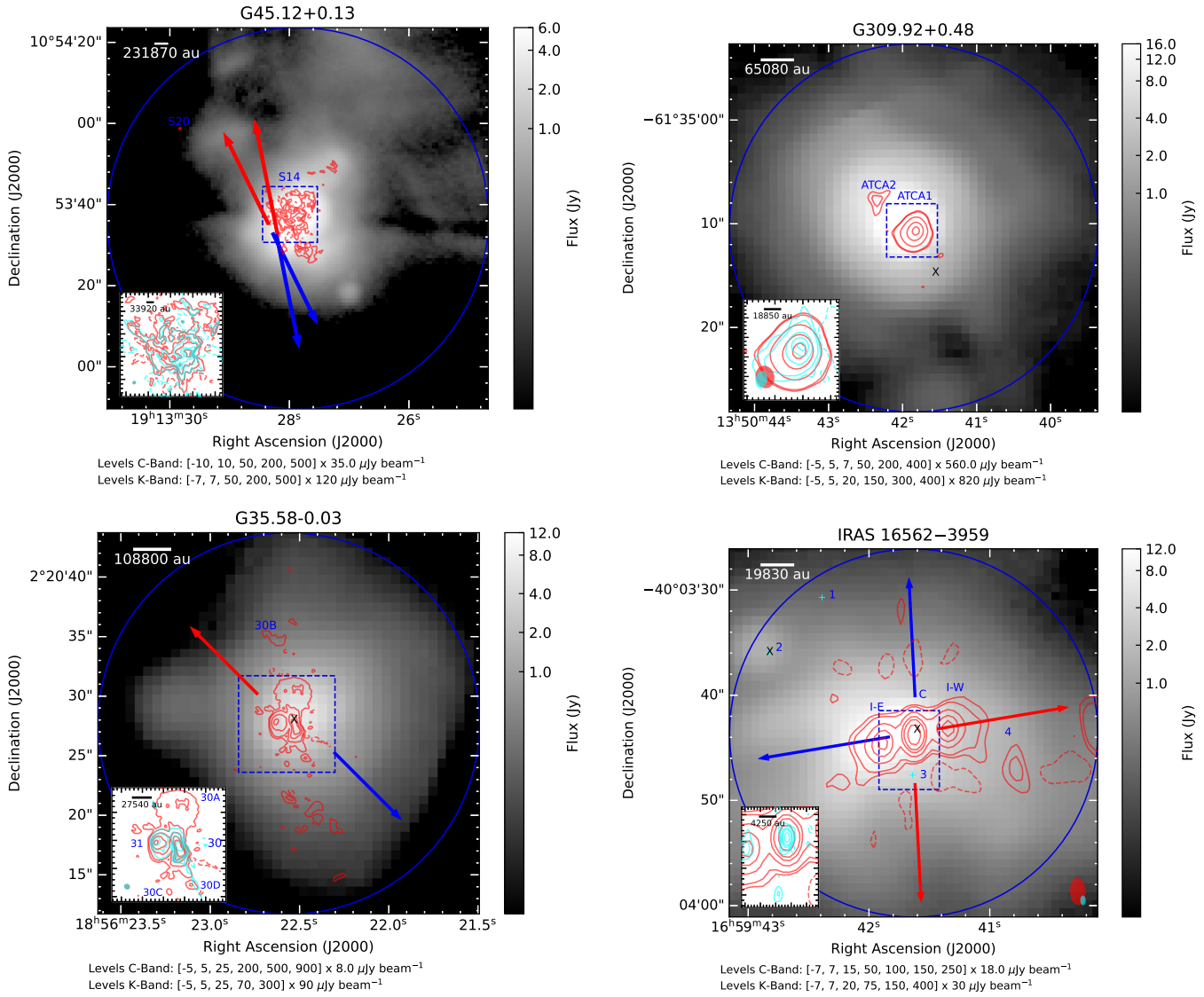

Figure 1. Images are SOFIA-FORCAST 37 μm (from SOMA II) with VLA contours—red: lower frequency (*C* band (6 cm) for the VLA observations and 5, 5.5 or, 7.2 GHz for ATCA observations); cyan: (*K* band (1.3 cm) for the VLA observations and 17, 19, or 19.9 GHz for ATCA observations)—of the combined radio maps overlaid. The centimeter emission observations for regions IRAS 16562–3959 and G339.88–1.26 are originally presented in A. E. Guzmán et al. (2016) and S. J. D. Purser et al. (2016), respectively. The cyan crosses in IRAS 16562–3959 denote the position of detections only at the high-frequency bands (cyan contours). The black × denotes the position of the millimeter core on the regions with millimeter observations (references as follows: G309.92+0.48: T. Hill et al. 2005, G35.58-0.03: C.-P. Zhang et al. 2014, IRAS 16562 3959: A. E. Guzmán et al. 2014, G305A: A. J. Walsh & M. G. Burton 2006, and G339.88-1.26: Y. Zhang et al. 2019a). The blue dashed squares correspond to the area of the inset image showing a zoom-in of the central region, and the synthesized beams are shown in the lower corners of these insets. The blue circles are the SOMA apertures used by SOMA V and reported in Table C1. The aperture radius is defined using the optimal aperture size algorithm developed by SOMA IV. The blue and red arrows represent the direction of a molecular outflow detected toward the region, only in regions with known molecular outflows (more details in Section 3.1). A scale bar in astronomical units is shown in the upper left of the figures.

data at the lowest-frequency observations (5.5 and 9.0 GHz) and at the highest-frequency observations (17 and 22.8 GHz). This resulted in two frequency-combined radio maps centered around 7.2 and 19.9 GHz, respectively.

For region IRAS 16562-3959, we used the data from A. E. Guzmán et al. (2016) at 5, 9, 17, and 19 GHZ: more information about the observations can be found in Section 2 of their paper. Meanwhile, for region G339.88-1.26, we used data from S. J. D. Purser et al. (2016) at 5.5, 9.0, 17.0, and 22.8 GHz: more information about the observations can be found in Section 3.1 of their paper. In order to have frequencies comparable to the combined images made for the other sources, we select the lowest- and highest-frequency maps of both regions for use in the direct comparison with the combined maps, but we used the images in the same way that they were published.

3. Results

Following the methods of SOMA Radio I, we consider a radio source being detected when the peak intensity I_ν is at least 5 times the rms (σ) in either of the baseband-combined images (see Sections 2.1 and 2.2) at the different frequencies. For nondetections in the combined images, we report an upper limit value of 3σ for the flux density at the given frequency.

Figure 1 shows the radio contour plots of the lower frequency in red (*C* band (6 cm) for the VLA observations and 5, 5.5, or 7.2 GHz for ATCA observations) and the higher

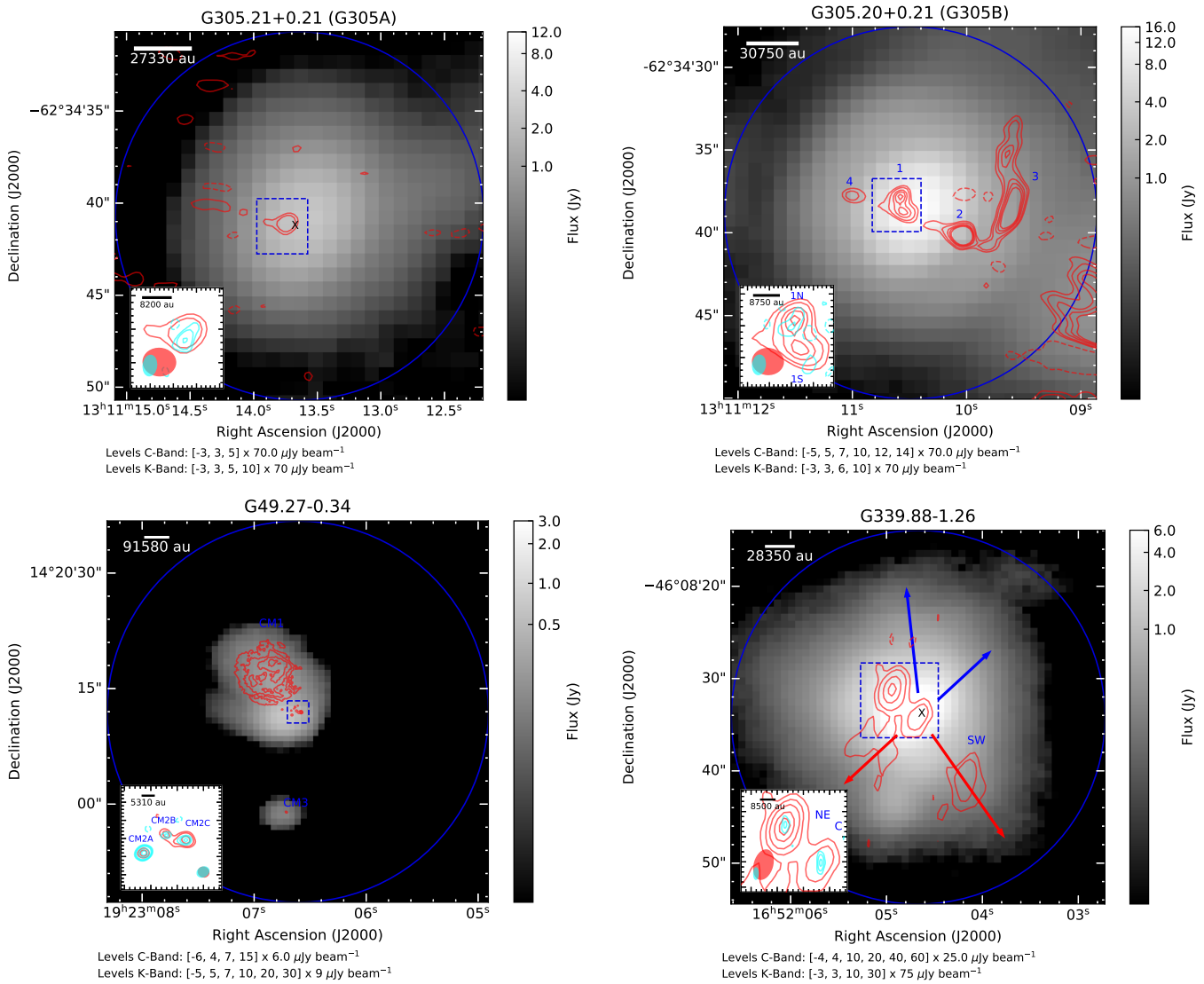

Figure 1. (Continued.)

frequency in cyan (*K* band (1.3 cm) for the VLA observations and 17, 19, or 19.9 GHz for ATCA observations) for all the radio sources detected in our sample and overlaid to SOFIA-FORCAST 37 μm images (from SOMA II).

The blue circles represent the SOMA aperture set by SOMA IV using the automated algorithm to choose the optimal aperture size (see Table C1 of SOMA V), except for IRAS 16562-3959 N, where the aperture radius is set from the 37.1 μm image reported by SOMA III (see Table 2 of SOMA III), this aperture size was used to build the IR SEDs. The infrared images presented in SOMA II (including SOFIA, Herschel, and Spitzer data) and the VLA data presented here have astrometric accuracies better than $1\farcs5$ and $0\farcs1$ (see Table 2), respectively. Meanwhile, the ATCA data presented here have astrometric accuracies better than $0\farcs4$, including both the phase calibrator's positional uncertainty and errors in transferring phases to the target.

Table 4 reports the radio parameters for each of the nine protostars studied in this paper. In line with the methods developed in SOMA Radio I, these parameters were measured based on different size scales, as follows. The SOMA scale refers to the size of the aperture radius used in SOMA II and SOMA V to measure IR fluxes. The intermediate scale is based on the morphology of the radio source, specifically whether the detections appear to be of jetlike nature. The inner scale is given by the size of the central radio detection that is likely most closely associated with the driving protostar, as set by the SOFIA data and the center of the infrared SEDs analyzed in SOMA II (i.e., association with compact millimeter dust continuum emission). For the VLA data presented, we determined the flux density S_ν in each wideband image in the SOMA and intermediate scales by using the task imstat of CASA, either enclosing the SOMA aperture in a circular region or enclosing the elongated jetlike structure in a box, respectively (see Table 5). The uncertainties of the flux densities for these two scales are estimated as $\sigma_{\rm image}(\rm npts/beam\ area)^{0.5}$ added in quadrature with an assumed 10% error in calibration, where $\sigma_{\rm image}$ is the rms of the image, npts is the number of pixels enclosed in the box or the circular region, and the beam area is the number of pixels within a synthesized beam of the image. For the inner scale, we determined the flux density using the task imfit of CASA,

Table 4
Parameters from Radio Continuum

Region	Scale	R.A (J2000)	Decl. (J2000)	$S_{5.0\ \mathrm{GHz}}$ (mJy)	$S_{7.0\ \mathrm{GHz}}$ (mJy)	$S_{20.4\ \mathrm{GHz}}$ (mJy)	$S_{24.4}$ GHz (mJy)	Spectral Index
	SOMA	19:13:27.86	+10:53:36.60	1797.44 (180.6)	1855.93 (186.5)	3673.00 (367.5)	3593.19 (360.71)	0.5(0.1)
G45.12+0.13	Intermediate	…	…	…	…	…	…	…
	Inner	19:13:27.87	+10:53:36.17	1702.69 (51.11)	1928.91 (57.89)	3668.96 (110.0)	3722.08(111.7)	0.5(0.1)
	SOMA	13:50:41.85	−61:35:10.40	454.76(47.4)	753.47(79.0)	1017.68 (108.6)	955.54(115.6)	0.5(0.1)
G309.92+0.48[a]	Intermediate	…	…	…	…	…	…	…
	Inner	13:50:41.84	−61:35:10.85	428.18(14.6)	713.91(29.3)	1085.90 (57.86)	1191.15(76.69)	0.7(0.1)
	SOMA	18:56:22.52	+02:20:27.20	172.38(17.3)	199.20(20.0)	302.12(30.6)	321.61(33.5)	0.4(0.1)
G35.58-0.03	Intermediate	…	…	…	…	…	…	…
	Inner [b]	18:56:22.52	+02:20:30.53	84.00(27.32)	118.00(35.05)	237.00(91.14)	263.00(101.47)	0.7(0.2)
	SOMA	16:59:41.63	−40:03:43.60	18.92(1.9)	23.50(2.4)	34.27(3.7)	31.56(3.5)	0.4(0.1)
IRAS 16562-3959[c]	Intermediate	16:59:42.17	−40:03:46.85	19.66(2.0)	27.63(2.8)	31.84(3.2)	33.34(3.4)	0.4(0.1)
	Inner	16:59:41.63	−40:03:43.73	8.18(0.87)	13.40(1.43)	20.80(2.19)	22.90(2.43)	0.8(0.1)
	SOMA	16:59:43.01	−40:03:11.56	<0.39	0.47(0.22)	0.59(0.64)	0.87(0.66)	<0.7
IRAS 16562-3959 N[c]	Intermediate	…	…	…	…	…	…	…
	Inner	…	…	<0.06	<0.06	<0.09	<0.08	<0.4
	SOMA	13:11:13.64	−62:34:40.70	1.25(2.37)	1.05(2.14)	0.71(2.18)	3.22(8.43)	−0.3(3.1)
G305.21+0.21[a]	Intermediate	…	…	…	…	…	…	…
(G305A)	Inner	13:11:13.75	−62:34:41.31	0.96(0.01)	0.74(0.04)	0.91(0.09)	2.70(0.27)	0.2(0.2)
	SOMA	13:11:10.49	−62:34:38.80	16.57(2.11)	12.98(2.36)	3.42(2.63)	<29.72	<−1.0
G305.20+0.21[a]	Intermediate	13:11:10.52	−62:34:39.08	7.23(0.83)	4.55(0.77)	1.59(0.83)	<9.33	<−1.2
(G305B)	Inner	13:11:10.56	−62:34:38.31	3.39(0.13)	1.61(0.89)	1.37(0.19)	1.92(0.38)	−0.7(0.2)
	SOMA	19:23:06.61	+14:20:12.00	44.30(4.54)	52.93(5.44)	26.11(3.34)	40.86(4.50)	−0.3(0.1)
G49.27-0.34[d]	Intermediate	19:23:06.69	+14:20:11.22	0.21(0.04)	0.01(0.04)	0.33(0.08)	0.34(0.07)	0.7(0.5)
	Inner	19:23:06.66	+14:20:11.66	0.04(0.01)	0.03(0.01)	0.27(0.02)	0.35(0.02)	1.6(0.2)
	SOMA	16:52:04.67	−46:08:34.20	5.50(0.71)	3.64(0.68)	4.11(2.16)	4.27(4.61)	−0.6(0.5)
G339.88-1.26[a]	Intermediate	16:52:04.62	−46:08:36.04	5.31(0.57)	6.86(0.73)	4.58(1.04)	4.03(2.05)	−0.1(0.2)
	Inner	16:52:04.94	−46:08:31.32	0.86(0.09)	1.51(0.16)	2.44(0.26)	3.00(0.33)	0.9(0.1)

Note. The intermediate scale corresponds to the extent of the radio jet (candidate). Units of R.A. are hours, minutes, and seconds. Units of decl. are degrees, arcminutes, and arcseconds.
[a] The frequencies at which the flux was measured were 5.5, 9.0, 17.0, and 22.8 GHz.
[b] The inner scale corresponds to source 30 that we are resolving into sources 30N and 30S (see Section 3.1.3 and Table 6 for more details). The following are ATCA observations.
[c] The frequencies at which the flux was measured were 5.0, 9.0, 17.0, and 19.0 GHz.
[d] The frequencies at which the flux was measured were 5.0, 7.0, 20.4, and 24.4 GHz.

and the uncertainty was estimated using the statistical error from the Gaussian fit added in quadrature with an assumed 10% error in calibration.

Columns (1) and (2) of Table 4 show the region and the given scale; for each, columns (3) and (4) report the R.A. and decl. For the SOMA scale, these refer to the pointing center observations of SOFIA-FORCAST (see SOMA II Table 1); for the intermediate scale, they refer to a middle point in the jetlike detection; and for the inner scale, they refer to the R.A. and decl. of the peak intensity of the central detected object. The following columns are the flux densities (S_ν) at different frequencies, with the uncertainties given in parentheses (for nondetections, the upper limits denote the minimum detectable flux of a point source). The last column in Table 4 reports the spectral indices and their uncertainties at each scale (see Section 3.2). Since we are limited by the LAS, the radio data are not sensitive to extended emission over scales as large as the SOMA and possibly the intermediate scales, the flux measurements represent the sum over all compact sources within the scale, and the spectral indices contain some corresponding uncertainty (more details in Section 3.2). The error bars for these measurements are large due to having many independent beams within the scale. Consequently, the uncertainties in the flux density and spectral index at these scales tend to be higher for some sources. It is important to note, however, that smaller structures such as the inner scale are less affected.

3.1. Morphology and Multiplicity

All the target regions presented in this paper have been observed in the centimeter continuum. Our criteria for multiplicity are the presence of two or more spatially resolved 5σ detections. Furthermore, we describe source morphology as

Table 5
Size Scales of Flux Measurements

Region	SOMA R ($''$)	Intermediate $w('') \times h(''$)	Inner $a(''$) × $b(''$)
G45.12+0.13	47.0	⋯	3.67 × 2.33[a]
G309.92+0.48	17.75	⋯	1.96 × 1.75[a]
G35.58-0.03	16.0	⋯	2.88 × 0.50[a]
IRAS 16562-3959	17.5	13.2 × 6.82	2.46 × 1.61[a]
IRAS 16562-3959 N	7.7	⋯	⋯
G305.20+0.21 A	10.0	⋯	1.16 × 1.11[a]
G305.20+0.21	11.25	8.68 × 4.45	1.12 × 0.77[a]
G49.27-0.34	24.75	2.01 × 1.14	0.44 × 0.37[b]
G339.88-1.26	20.25	13.8 × 17.9	2.38 × 0.91[a]

Note. The reported values correspond to a circle of radius R for the SOMA scale and a box of height h and width w for the intermediate scale. In some cases, the inner scales of the C- and K-band images differ. In these situations, we report the larger area and consider any emission within the inner region. We also distinguish between two types of regions:
[a] Scale corresponds to image component (convolved with beam) size from the task imfit, of major axis a and minor axis b.
[b] Scale corresponds to an ellipse of major axis a and minor axis b.

"compact" if the detection shows no structure on the scale of a few synthesized beams or greater. Otherwise, we describe it as "extended." Below, we describe the centimeter wavelength detections toward each target; for a detailed literature review on each of these regions, see SOMA II.

3.1.1. G45.12+0.13

G45.12+0.13 is a massive star-forming region, also known as IRAS 19111+1048, that is associated with an ultracompact (UC) H II region. It is located at 7.4 kpc (A. Ginsburg et al. 2011) and is part of the Galactic Ring Survey Molecular Cloud G45.46+0.05, a large star formation complex (D. O. S. Wood & E. Churchwell 1989; R. Simon et al. 2001).

G45.12+0.13 has been analyzed at multiple wavelengths, ranging from IR, submillimeter, and radio (T. R. Hunter et al. 1997; S. Vig et al. 2006; A. Y. Yang et al. 2021; N. Azatyan et al. 2022). T. R. Hunter et al. (1997) reported bipolar outflows toward this region using CO (J = 6–5) maps. From this study, the highest-velocity outflow is centered around a source termed S14, while an additional outflow is centered around another UC H II region source, G45.12+0.13 West. Both of these UC HII regions contain type-I OH masers (A. L. Argon et al. 2000). Additionally, with radio observations from the Giant Metrewave Radio Telescope (GMRT) at 1280, 610, and 325 MHz, S. Vig et al. (2006) suggested that this region shows a highly homogeneous ionized medium morphology, and SOMA II confirms this morphology with their mid-IR (MIR) images. Furthermore, S. Vig et al. (2006) concluded that G45.12+0.13 contains a cluster of zero-age main-sequence (ZAMS) stars energizing a compact and evolved H II region. In total, they reported 20 sources, with S14 being the central UC H II source and S20 a nonthermal source according to its radio emission.

From our VLA observations at 1.3 and 6 cm, we report two detections corresponding to sources S14 and S20 from S. Vig et al. (2006). Both detections have an offset in the peak intensity position from the results of S. Vig et al. (2006) using GMRT observations, by a difference of around $2\farcs1$ to the SE (see Figure 2). This systematic offset may be due to astrometric uncertainties in the GMRT data, for which we do not have enough information to quantify. Contributions to the uncertainty are expected to include calibrator position, phase transfer, and self-calibration. The peak can also change with resolution, given the presence of extended components.

It is important to highlight that despite our data being of higher resolution, we only detect 2 of the 20 compact sources from the cluster reported by S. Vig et al. (2006). From our data, we infer that most of the emission to the northern side of the central UC H II region arises from an extended and diffuse irregular cloud of ionized material instead of a cluster of compact sources. The presence of a position offset does not change this conclusion.

In order to confirm our results, we produce an image using shorter baseline observations from the VLA archive (project code 20A-519; PI: David Neufeld) at the L band (1.5 GHz) in order to compare the results with the 1.28 GHz image from S. Vig et al. (2006). Figure 2 shows this L-band continuum image with overlaid C-, K-, and L-band VLA contours. The positions of the cluster of point sources reported by S. Vig et al. (2006) at 1280 MHz are marked with white × symbols.

Based on these results, we clearly see that from our images at 1.3 and 6 cm (see Figure 1), the diffuse ionized material has been filtered out by the long baselines; hence, we only detect the very compact point source S20 and the most inner part of the UC H II region source S14. Furthermore, from the shorter baseline image, we infer that most of the emission to the north west of the central UC H II region arises from an extended and diffuse irregular cloud of ionized material instead of a cluster of compact sources.

From our VLA observations, source S14 is located at R.A.(J2000) = $19^{h}13^{m}27\fs87$, decl.(J2000) = $+10°53'36\farcs2$ with a spectral index of 0.5. S14 presents a very complex morphology, and in fact, at the shorter frequency (L band), it appears to have an hour-glass morphology, as seen in the right plot of Figure 2. This observed morphology is similar to the one detected toward source G45.47+0.05 by Y. Zhang et al. (2019b), who interpreted this as arising from a photoionized outflow. Furthermore, the molecular outflows observed toward G45.12+0.13 (see Figure 1) are consistent with the direction of the axis of the hourglass of source S14.

Meanwhile S20 is located at R.A.(J2000) = $19^{h}13^{m}29\fs83$, decl.(J2000) = $+10°53'58\farcs7$, presents a very compact morphology at both frequency bands and a spectral index of −0.9, a value that is consistent with the nonthermal detection made by S. Vig et al. (2006). Moreover, S. Vig et al. (2006) concluded that, even though source S20 is in the vicinity of G45.12 +0.13, it is not likely to be associated with the UC HII region. If this source is indeed independent, the nature of this source could be extragalactic, but more information and observations to confirm this assessment are needed.

3.1.2. G309.92+0.48

G309.92+0.48 or IRAS 13471-6120 is a region located at 5.5 kpc (T. Murphy et al. 2010). It is associated with OH and methanol masers, as well as radio continuum emission from an UC H II region at several radio observations ranging from 5 to 24 GHz (J. L. Caswell 1997; C. J. Phillips et al. 1998; A. J. Walsh et al. 1998; A. L. Patel et al. 2025). A. Y. Yang et al. (2021, 2022) reported a CO molecular outflow toward this region. In the MIR, G309.92+0.48 is resolved into several sources: J. M. De Buizer et al. (2000) reported it to be

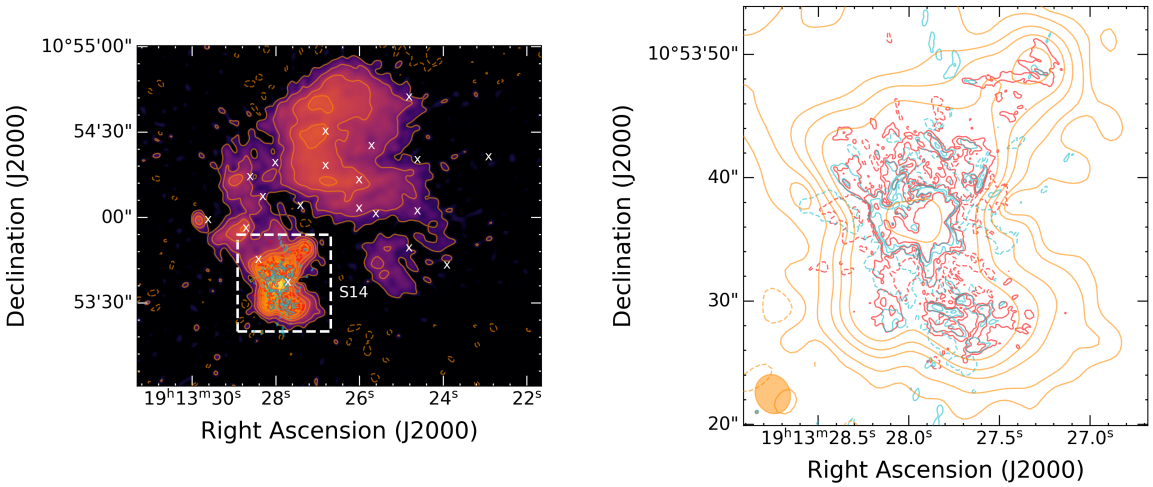

Figure 2. Left: *L*-band VLA (20 cm) continuum maps with VLA contours overlaid (1.3 cm–cyan, 6 cm–red, 20 cm–orange) of G45.12+0.13. The white × symbol is the location of the sources in the cluster reported by S. Vig et al. (2006). Note the offset in the peak intensity position from the results of S. Vig et al. (2006) with respect to the VLA observations. Right: zoom region of source S14 with the VLA contours of the three bands. The contour levels are at [−5, 5, 20, 100] × 35 μJy beam^{-1} for the *C* band, at [−5, 5, 15] × 120 μJy/beam for the *K* band, and at [−3, 3, 10, 30, 55, 100, 300, 500] × 0.25 mJy beam^{-1} for the *L* band. The synthesized beams are shown in the lower left corner.

composed of a total of six point sources (labeled 1–6) using high-resolution (∼0.″3) 11.7 μm data from Gemini (see also SOMA II).

From our ATCA observations, we have detected two sources that we name ATCA1 and ATCA2 (see Figure 1). Source ATCA1 is detected at all frequencies (5.5, 9, 17, and 22.8 GHz), and source ATCA2 is only detected at the lower frequencies (5.5 and 9 GHz). Both sources are consistent with the previously reported sources by C. J. Phillips et al. (1998) at 8.6 GHz, sources that are associated with the MIR sources 1 and 2. T. Murphy et al. (2010) presented radio continuum observations at 20 GHz toward this region, detecting only source ATCA1, which is consistent with our results of nondetection for source ATCA2 at higher frequencies.

ATCA1 is a slightly elongated source located at R.A.(J2000) = $13^{h}50^{m}41\overset{s}{.}84$, decl.(J2000) = −61°35′10.″8 and we report a spectral index of 0.7. ATCA2 is located at R.A.(J2000) = $13^{h}50^{m}42\overset{s}{.}29$, decl.(J2000) = −61°35′07.″7 with a spectral index of −0.7. Both of these sources show a similar morphology to the previous radio observations mentioned above.

For ATCA1, T. Murphy et al. (2010) reported a spectral index of 1.2 between 0.843 and 20 GHz, and A. L. Patel et al. (2025) reported a spectral index of 0.5 between 5 and 24 GHz. Our estimated value (∼0.7) is similar to the one reported by A. L. Patel et al. (2025) at similar frequencies. The estimated spectral index value is consistent with either a typical UC H II region (I. E. Kalcheva et al. 2018) or collimated ionized jets (S. P. Reynolds 1986; S. J. D. Purser et al. 2016, 2021). Based on our results, we classify this source as an optically thick thermal emitter. However, we cannot rule out the possibility of a radio jet, since masers and molecular outflows have been reported toward this source, and a nearby nonthermal component is present. ATCA2, on the other hand, exhibits nonthermal emission, with an upper limit of $\alpha < -0.7$, and shows slight extension, as seen in Figure 1. The nature of this source remains uncertain: given the large distance to this region and the observed morphology, an extragalactic origin cannot be ruled out. Alternatively, this source could represent a jet lobe if ATCA2 was indeed a radio jet. Additional information is required to make a more definitive assessment of the nature of this source.

3.1.3. G35.58-0.03

G35.58-0.03 (hereafter G35.58) is a star-forming region located at a kinematic distance of 10.2 kpc (C. Watson et al. 2003). G35.58 has been resolved into two UC H II regions (from now on called sources 30 and 31) using 2 and 3.6 cm observations, where water and OH masers have been detected toward source 30 (S. Kurtz et al. 1994; J. L. Caswell et al. 1995). Additionally, C.-P. Zhang et al. (2014) show evidence of an ionized outflow driving a NE–SW molecular outflow centered in source 30.

With high-resolution 11.7 μm Gemini observations, SOMA II resolved the MIR emission into a main bright peak with two extended diffuse emissions to the north and the northwest. The main bright peak is associated with the eastern UC H II region (source 31).

We present 6 and 1.3 cm observations of this region, where we detect twelve sources at different evolutionary stages. Most of these sources are only detected at the *C* band, with a few sources being detected at both frequency bands (30A, 30E, 30N, 30S, and 31). Table 6 shows the information about the multiplicity in G35.58, such as the R.A. and decl. positions, the estimated spectral indices, association with other wavelengths, and whether the source is a new radio detection or not.

G35.58-0.03 30 and 31. Sources 30 and 31 have previously been referred to as UC H II regions (e.g., S. Kurtz et al. 1994). For source 31, based on its morphology in the centimeter and its estimated spectral index, we agree that its nature is a UC H II region. Moreover, source 31 appears to already have a central protostar based on its association with a bright and compact MIR source (SOMA II).

From our observations, source 30 shows a double peak at the *C* band and a single peak at the *K* band. At lower frequencies, we marginally resolve it into two components, labeled 30N and 30S (Figure 3), aligned roughly NE–SW, consistent with the larger-scale molecular outflow previously observed in the region. This, together with their association

Table 6
Multiplicity in G35.58-0.03

Source	R.A (J2000)	Decl. (J2000)	Spectral Index	Association	New Detection
30A	18:56:22.52	+02:20:30.5	0.7(0.1)	IR	Yes[a]
30B	18:56:22.62	+02:20:34.7	<−1.1	⋯	Yes[b]
30C	18:56:22.57	+02:20:24.3	<−0.3	⋯	Yes[b]
30D	18:56:22.47	+02:20:24.8	<−1.2	⋯	Yes[b]
30E	18:56:22.55	+02:20:21.4	−0.5(0.1)	⋯	Yes[b]
30F	18:56:22.43	+02:20:20.5	<−0.5	⋯	Yes[b]
30G	18:56:22.39	+02:20:19.7	<−1.0	⋯	Yes[b]
30H	18:56:22.46	+02:20:18.9	<−1.9	⋯	Yes[b]
30J	18:56:22.19	+02:20:21.5	<0.6	⋯	Yes[b]
30K	18:56:22.19	+02:20:21.5	<0.1	⋯	Yes[b]
30N	18:56:22.53	+02:20:27.6	−0.5(0.4)	IR, millimeter	Yes[c]
30S	18:56:22.52	+02:20:27.2	0.2(0.1)	IR, millimeter	Yes[c]
31	18:56:22.62	+02:20:27.9	0.0(0.1)	MIR, millimeter	No

Note. Units of R.A. are hours, minutes, and seconds. Units of decl. are degrees, arcminutes, and arcseconds.
[a] These sources have been previously detected at different wavelengths but not in the radio continuum.
[b] These sources have been previously observed but not detected.
[c] These sources have been previously detected in radio continuum, but we are resolving them into multiple detections.

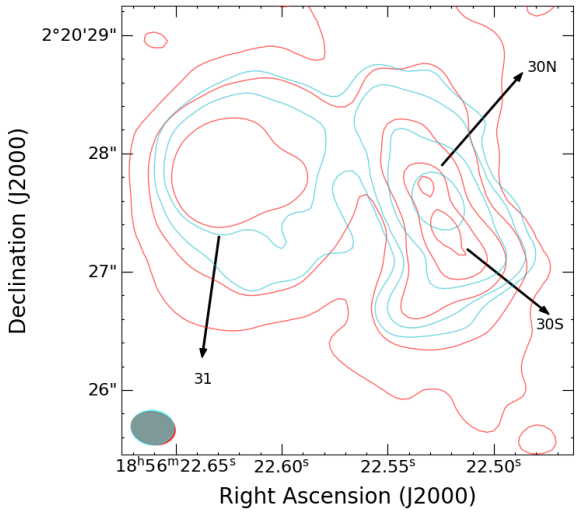

Figure 3. VLA continuum maps of the triple system toward G35.58-0.03 observed at 1.3 and 6 cm. The beam sizes are indicated in the lower left-hand corner. The contour levels are at $\sigma \times (-10, 10, 100, 500, 1200, 1700)$ for the *C* band (red) and $\sigma \times (-10, 10, 25, 100, 500)$ for the *K* band (cyan), with the σ value reported in Table 1.

with water maser, suggests that 30N and 30S could trace an ionized jet. The estimated spectral index of ∼0.7, derived from the inner scale encompassing source 30, is consistent with typical values for ionized jets associated with young stellar objects (YSOs; e.g., S. P. Reynolds 1986; G. Anglada et al. 1998; K. E. I. Tanaka et al. 2016). In Table 6, we also provide estimates of the spectral indices for 30N and 30S. However, higher-resolution observations will be required to confirm the jet scenario. Finally, the association with multiple star formation tracers further suggests that source 30 may be in a younger evolutionary stage than source 31.

G35.58-0.03 30A. Source 30 A appears in the MIR observations as two-pronged diffuse emission in the northern direction (SOMA II). We have detected, for the first time, associated centimeter emission with a bubble-like morphology.

G35.58-0.03 30B-30K. Sources 30B to 30K are presented in Figures 1 and 4. To our knowledge, these are new weak radio detections (for more details, see Table 6). The majority of the sources are only detected at the *C* band, except for 30E, which is detected at both the *C*- and *K*-bands. Figure 4 is centered ∼ 2.″2 to the SW of the SOMA scale (coordinates in Table 1).

These new sources present a variety of morphologies: mostly compact sources, but with some of them slightly extended. Upper limit estimates of the spectral indices indicate that all these new sources, except for 30J, are consistent with synchrotron emission. Given their slight alignment with the direction of the molecular outflow, these sources may be part of an ionized jet that is being driven by source 30, which is itself elongated in the same direction.

Despite our suggested classification of an ionized jet for source 30, defining an intermediate scale for this source is not feasible. The extent of the presumed jet is already enclosed within the SOMA scale, with the caveat that this scale contains the UC H II region in source 31 and the bubble-like morphology of source 30A. Any intermediate scale would face the same issue; therefore, we omitted this scale for this particular case.

The high multiplicity observed in this region raises the question of whether these detections are real or artifacts. In general, we expect artifacts to exhibit symmetric properties, but, as shown in Figures 1, 3, and 4, we can see that this is not the case for most of our detections. Furthermore, based on estimates of calibration and deconvolution errors, we find that source 30B is at least 25 times brighter than what would be expected for a point-spread function artifact. This implies that detections at least 10 times fainter than source 30B could plausibly be artifacts. Among our sources, this criterion only applies to source 30J, which is approximately 10 times fainter than source 30B. Therefore, we conclude that most of our detections are likely real.

3.1.4. IRAS 16562-3959

IRAS 16562-3959, also known as G345.49+1.47, is located at a distance of 1.7 kpc and hosts a massive core containing a massive star in an early stage of evolution (A. E. Guzmán et al. 2010). A. E. Guzmán et al. (2011) reported a quadrupolar

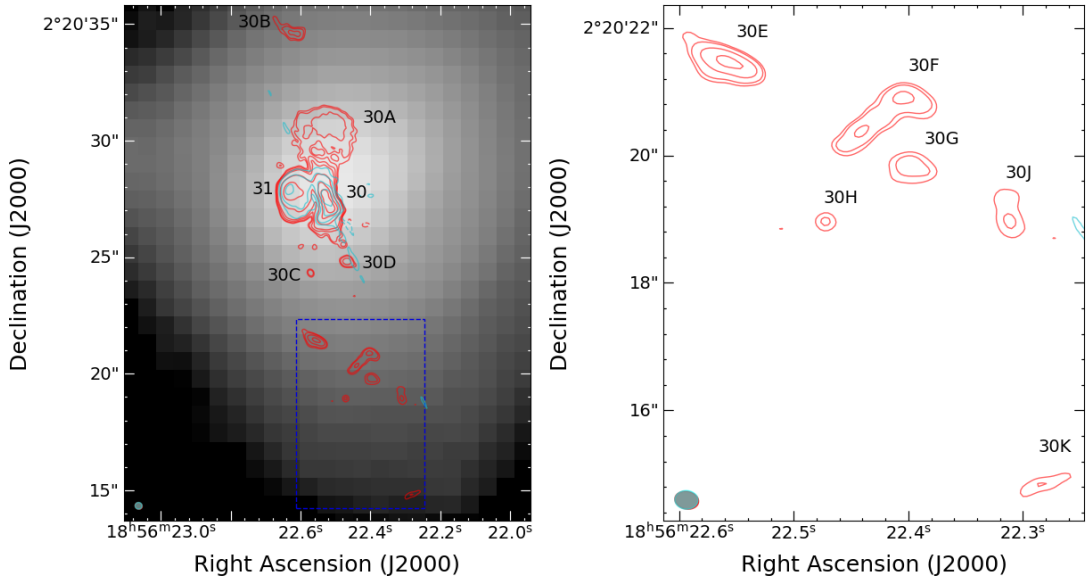

Figure 4. VLA continuum 1.3 and 6 cm maps showing the multiplicity of region G35.58-0.03 in the SW of the SOMA scale. The beam sizes are indicated in the lower left-hand corner. The contour levels are at $\sigma \times (-8, 8, 11, 20, 35)$ for the *C* band and $\sigma \times (-5, 5, 10)$ for the *K* band, with the σ value reported in Table 1.

molecular outflow traced by CO. This morphology is explained by the presence of two collimated bipolar outflows, one lying in the SE–NW direction related to the ionized jet detected by A. E. Guzmán et al. (2010), and another in the N–S direction that could be related to the unresolved millimeter source 13 in A. E. Guzmán et al. (2014).

For our analysis, we used A. Guzman's ATCA observations at 5.5, 9, 17, and 19 GHz from A. E. Guzmán et al. (2016), where they reported nine radio detections associated with this region. The central source has a counterpart at 3 mm and X-rays (source 10 at 3 mm and source 161 in X-rays; A. E. Guzmán et al. 2014; V. A. Montes et al. 2020), and has also been detected in the MIR by the SOMA II study.

We focus on the regions IRAS 16562-3959 and IRAS 16562-3959 N. The latter was added to the sample in SOMA III due to the detection of a point source in the IR maps, based on the observations analyzed in SOMA II.

IRAS 16562-3959. For the purpose of this study, we only focus on the sources within the SOMA scale (see Figure 1). Detections C, I-E, and I-W all exhibit compact morphologies. As described by A. E. Guzmán et al. (2014), this region shows characteristics consistent with an ionized radio jet, driven by the central free–free emission source (C) and accompanied by two lobes (I-E and I-W) of nonthermal emission. Given the clear jetlike morphology, we also measure the fluxes using an intermediate scale, as previously described, that encompasses the central source (detection C) and the two inner radio lobes.

Sources 1, 2, and 3 exhibit compact morphologies. A. E. Guzmán et al. (2016) discuss the nature of these detections in Section 4.2.2 of their paper. In summary, source 1 may be extragalactic, source 2 is likely a hypercompact (HC) H II region associated with a young high-mass star, and the free–free emission from source 3 originates from a low-mass YSO.

Based on our criteria, and for completeness, we report all detections above a 5σ threshold, adopting the same signal-to-noise ratio definition as A. E. Guzmán et al. (2016). As a result, we identify a new source, source 4 (following the convention of A. E. Guzmán et al. 2016), which is detected only at 5 and 9 GHz, shows a slight elongation to the south (Figure 1), and was not previously reported. We estimate an upper limit to its spectral index of $\alpha < 1.3$.

IRAS 16562-3959 N. In these observations, we were not able to detect source IRAS 16562-3959 N, which is an MIR source reported by SOMA III as a secondary region around IRAS 16562-3959. This point source was detected using IR data, and, moreover, we see this new detection at the shortest wavelengths (MIR), but not in the longest wavelengths (far-IR; FIR) of the observations analyzed in SOMA II.

3.1.5. G305.20+0.21

The G305.2+0.2 complex is a vast high-mass star-forming region located at a distance of 4.1 kpc (V. Krishnan et al. 2017) in the southern Galactic plane. Within the region, there are two locations separated by 22″ named G305A (G305.21+0.21) and G305B (G305.20+0.21), where Class II methanol (CH^3OH) masers have been detected (R. P. Norris et al. 1993; A. J. Walsh & M. G. Burton 2006; A. J. Walsh et al. 2007). Additionally, G305C has been recently reported by SOMA II as an IR source located at 14″ to the east of G305B, and it is detected at all SOFIA wavelengths, showing NIR counterparts, as well.

From previous radio continuum observations toward G305.20+0.21, there are reports of two detections, which are prominent extended H II regions labeled as G305HII(SE) and G305HII by A. J. Walsh et al. (2007). These regions are located about 30″ to the SE of G305A and 15″ to the SW of G305B, respectively (C. J. Phillips et al. 1998; A. J. Walsh et al. 2007).

Figure 1 shows the observations toward this region, where the centimeter data images were made using a minimum baseline length of 1.5 km. The main reason for doing this was to improve the detections of the compact radio emission associated with G305A and G305B, which are our sources of interest, by filtering out the bright, extended emission from the two H II regions (i.e., G305HII(SE) and G305HII) located to the south of each of them.

Table 7
Multiplicity in G305.20+0.21 (G305B)

Source	R.A (J2000)	Decl. (J2000)	Spectral Index	Association	New Detection
G305B ATCA-1N	13:11:10.58	−62:34:37.8	<0.4	IR	Yes[a]
G305B ATCA-1S	13:11:10.56	−62:34:38.8	<−1.0	IR	Yes[a]
G305B ATCA-2	13:11:10.04	−62:34:40.1	−0.8(0.2)	⋯	Yes[b]
G305B ATCA-3	13:11:09.63	−62:34:38.7	−0.6(0.2)	⋯	Yes[b]
G305B ATCA-4	13:11:10.99	−62:34:37.8	<−1.7	⋯	Yes[b]

Note. Units of R.A. are hours, minutes, and seconds. Units of decl. are degrees, arcminutes, and arcseconds.
[a] These sources have been previously detected at different wavelengths but not in the radio continuum.
[b] These sources have been observed but not detected.

G305A (G305.21+0.21). This source is prominent at MIR and FIR (SOMA II) and has been observed at 8.6 and 18 GHz, but no radio detections have been reported at sensitivity levels of 0.9 mJy and 0.22 mJy, respectively (C. J. Phillips et al. 1998; A. J. Walsh et al. 2007). With our ATCA observations at 5.5, 9, 17, and 22.8 GHz, we report a single detection within the region G305A that we label as G305A ATCA-1 (see Figure 1: G305.21+0.21 (G305A)). This source coincides with the methanol maser reported by A. J. Walsh & M. G. Burton (2006) and shows a slight elongation at the lower frequencies. A. Y. Yang et al. (2021, 2022) reported CO molecular outflows toward this region in the ATLASGAL clump scale.

For G305A, we report an estimated spectral index of $\alpha \sim 0.3$, a result that indicates thermal emission. SOMA II suggested that G305A is a much younger and more embedded source than G305B and in a hot core phase, rich in molecular tracers (A. J. Walsh et al. 2007). Considering the spectral index value and star formation tracers such as reported masers and molecular outflows, we suggest that this source is most likely a radio jet.

G305B (G305.20+0.21). Region G305B is the brightest MIR source, and it is associated with methanol masers. However, no radio emission has been previously detected toward this region (A. J. Walsh et al. 2007). In our ATCA observations (see Figure 1), we report four sources labeled G305B ATCA-1, G305B ATCA-2, G305B ATCA-3, and G305B ATCA-4 (hereafter, sources 1, 2, 3, and 4). In Table 7, we present more information about the multiplicity in G305B, such as the R.A. and decl. positions, the estimated spectral index, association with other wavelengths, and whether this source is a new radio detection or not.

Source 1 is the main detection in the region, and in our ATCA observations, this source is seen at all frequencies (5.5, 9, 17, and 22.8 GHz) and exhibits a morphology with a slight elongation in the NE–SW direction. SOMA II was able to resolve this source into two sources (G305B1 and G305B2) using high-spatial-resolution Gemini observations, finding morphologies that are also aligned in the NE–SW direction. They suggested that both sources are part of an outflow cavity. In our ATCA observations at the lowest frequencies (5.5 and 9 GHz), source 1 has two peaks, 1N and 1S (see inset in Figure 1), that appear to be associated with their MIR counterpart. Our global spectral index estimate of source 1 is dominated by nonthermal emission ($\alpha = -0.7$), suggesting the existence of a high-speed jet in the region. Given the orientation of the sources, the driving source of this jet is likely source 1N, which is the brightest source, and we estimate a rough spectral index of $\alpha \sim 0.4$.

To our knowledge, sources 2, 3, and 4 are also new detections in the radio continuum. Source 2 is seen in all our ATCA observations and, similarly to source 1, shows a slight elongation in the NE direction and exhibits a spectral index that indicates nonthermal emission.

Source 4 is a faint compact eastern source only seen at the lowest frequencies (5.5 and 9 GHz), and we report a limit on its spectral index (see Table 7). On the other hand, source 3 is seen at all frequencies and presents an elongated morphology in the SE–NW direction that appears as a double peak at the longest contour levels shown in Figure 1. This source may be part of the H II region in A. J. Walsh et al. (1999), but in our observations, we report it as an independent source. We report a negative spectral index ($\alpha \sim -0.6$), suggesting nonthermal emission.

Since sources 2 and 4 are aligned in the same SW–NW direction, exhibit relatively compact morphologies and negative spectral indices, we conclude that the most likely nature of these sources is that they are nonthermal knots, centered in source 1N. Following our convention for sources with jetlike morphology, we measured the flux densities at an intermediate scale that encompasses the central source and the jet knots (sources 1, 2, and 4). At this scale, we estimate an upper limit on the spectral index of $\alpha < -1.2$, which is indicative of a nonthermal jet in the region.

Additionally, source G305C is within the SOMA scale for region G305B, but we are not detecting any radio source at our sensitivity levels. It is important to highlight that due to the minimum baseline length used in our images toward these regions, the flux measured for the SOMA scale corresponds to a lower limit, especially for source G305B, due to the proximity to the H II region, which has been filtered out in our images.

3.1.6. G49.27-0.34

G49.27-0.34 is a protostar located in an infrared dark cloud at a kinematic distance of 5.55 kpc (C. J. Cyganowski et al. 2009). To our knowledge, no molecular outflow has been detected toward this region to date. Two Class I 44 GHz CH^3OH maser spots have been detected in this region, while no 6.7 GHz CH^3OH, 25 GHz CH^3OH, or thermal masers have been detected (C. J. Cyganowski et al. 2009; A. P. M. Towner et al. 2017).

In our 1.3 and 6 cm observations, we report five detections within the SOMA scale. Table 8 shows some information about the multiplicity in G49.27-0.34, i.e., the coordinates, estimated spectral index, association at other wavelengths, and whether or not a source is a new radio detection. We discuss each detection below.

Table 8
Multiplicity in G49.27-0.34

Source	R.A (J2000)	Decl. (J2000)	Spectral Index	Association	New Detection
CM1	19:23:06.87	+14:20:17.3	0.8(0.1)	IR	No
CM2A	19:23:06.66	+14:20:11.6	1.6(0.2)	IR	Yes[a]
CM2B	19:23:06.62	+14:20:12.1	>0.7	IR	Yes[a]
CM2C	19:23:06.58	+14:20:11.9	0.0(0.1)	IR	Yes[a]
CM3	19:23:06.71	+14:19:59.0	<0.5	IR	Yes[b]

Note. Units of R.A. are hours, minutes, and seconds. Units of decl. are degrees, arcminutes, and arcseconds.
[a] These sources have been previously detected in radio continuum, but we are resolving them into multiple detections.
[b] These sources have been previously detected at different wavelengths but not in the radio continuum.

CM1. Source CM1 is an extended source previously seen at 1.3, 3.6, and 20 cm (D. M. Mehringer 1994; C. J. Cyganowski et al. 2011; A. P. M. Towner et al. 2017), and it is coincident with MIPS 24 μm emission (S. J. Carey et al. 2009). There are no reports of association with Class I 44 GHz CH^3OH masers.

C. J. Cyganowski et al. (2011) suggest that CM1 is a single ionizing star of spectral type B0V based on optically thin free–free emission and the ionizing photon flux. Our 1.3 cm flux density values are 1 order of magnitude less than those reported by C. J. Cyganowski et al. (2011) and A. P. M. Towner et al. (2017) with VLA observations and resolutions of $\sim 0\farcs8$ (2.63 and 1.62 mJy). This difference is likely due to the different resolutions.

CM2. The MIR peak observed in SOMA II is associated with source CM2, previously reported as an unresolved, 4σ detection at 0.027 mJy beam^{-1} rms at 3.6 cm (C. J. Cyganowski et al. 2011). Additionally, C. J. Cyganowski et al. (2011) estimated a spectral index limit of <0.2 at a resolution of $\sim 0\farcs9$. Using our VLA data, we are able to resolve source CM2 into three components, which we have labeled as CM2A, CM2B, and CM2C, with all sources detected at both 1.3 and 6 cm observations.

CM2A is the central and brightest source at 1.3 cm among the components of CM2. It shows a compact morphology and a very steep spectral index of 1.6.

CM2B is detected as an unresolved source, located $\sim 0\farcs7$ SW of the central component (CM2A), and it is the weakest detection in this system. We estimated a lower limit for the spectral index of 0.7.

CM2C is located about $1\farcs2$ of the central component in the same direction as CM2B. It presents a compact morphology with a flat spectral index suggesting thin free–free emission.

Given the extended morphology of the CM2A-CM2C sources at low frequencies, we also measure the flux densities using an intermediate scale that incorporates the three components. The estimated spectral index at this scale yields a value of 0.7, an indication that CM2 could be a radio jet with CM2A being the driven source of this jet.

CM3. From the contour maps in C. J. Cyganowski et al. (2011) and A. P. M. Towner et al. (2017), source CM3 shows MIPS 24 μm emission, and SOMA II also detected this source in the SOFIA IR maps, but not in the NIR. This source has no previous radio detections at 1.3 and 3.6 cm. In our observations, we are able to detect this source, but only at 6 cm (*C* band).

CM3 exhibits a compact morphology, and we report a relatively flat spectral index with an upper limit of 0.5, indicative of thermal emission. To our knowledge, we are detecting this source for the first time in radio frequencies, and its naming follows the convention of the main region, G49.27-0.34. This source may be a YSO at a more evolved stage than CM2, although additional observations are required for a definitive assessment.

3.1.7. G339.88-1.26

G339.88-1.26 (or IRAS 16484-4603) is a massive protostar located at 2.1 kpc (V. Krishnan et al. 2015) that has been previously observed at a variety of wavelengths. J. M. De Buizer et al. (2002) resolved the central MIR emission into three peaks (1A, 1B, and 1C) and radio continuum observations have identified the central source is associated with a radio jet and the other two sources are associated with radio outflow lobes (S. P. Ellingsen et al. 1996; S. J. D. Purser et al. 2016), label as C, NE and SW. Using Atacama Large Millimeter/submillimeter Array data, Y. Zhang et al. (2019a) reported two molecular outflows toward this region positioned at the source C. One of these outflows is located in the NE–SW orientation and exhibits the same angle as the ionized outflow reported by S. J. D. Purser et al. (2016).

With 19.7 μm SOFIA data, both molecular outflows are detected; however, at longer wavelengths, only the molecular outflow associated with the ionized outflow is observed. SOMA II suggests this could be due to extinction, and that the detection of red and blueshifted emission on both sides suggests a near side-on view of the outflows.

For our analysis, we used the ATCA observations at 5.5, 9.0, 17.0, and 22.8 GHz reported by S. J. D. Purser et al. (2016). We focus on the three sources within the SOMA scale, i.e., NE, C, and SW, identified by S. J. D. Purser et al. (2016). Source C appears compact at higher frequencies but shows a slight extension at lower frequencies, particularly at 5.5 GHz. In contrast, sources NE and SW exhibit relatively compact morphologies, with source SW being especially compact.

As mentioned by S. J. D. Purser et al. (2016), source G339.88-1.26 shows characteristics consistent with an ionized radio jet driven by the central source C and two lobes of nonthermal emission. Given this jetlike morphology of the region, we also measure the flux densities using an intermediate scale that encompasses the three sources. We report a spectral index of $\alpha \sim -0.1$ for the intermediate scale, suggesting that the nonthermal emission from the lobes is more prevalent at this scale.

3.2. Radio SEDs

Building upon the results of SOMA II, in Figure 5 we present the E-SEDs, i.e., radio + IR SEDs, for our nine protostellar sources. The dashed lines correspond to the best fit to the radio continuum data using a power law of the form

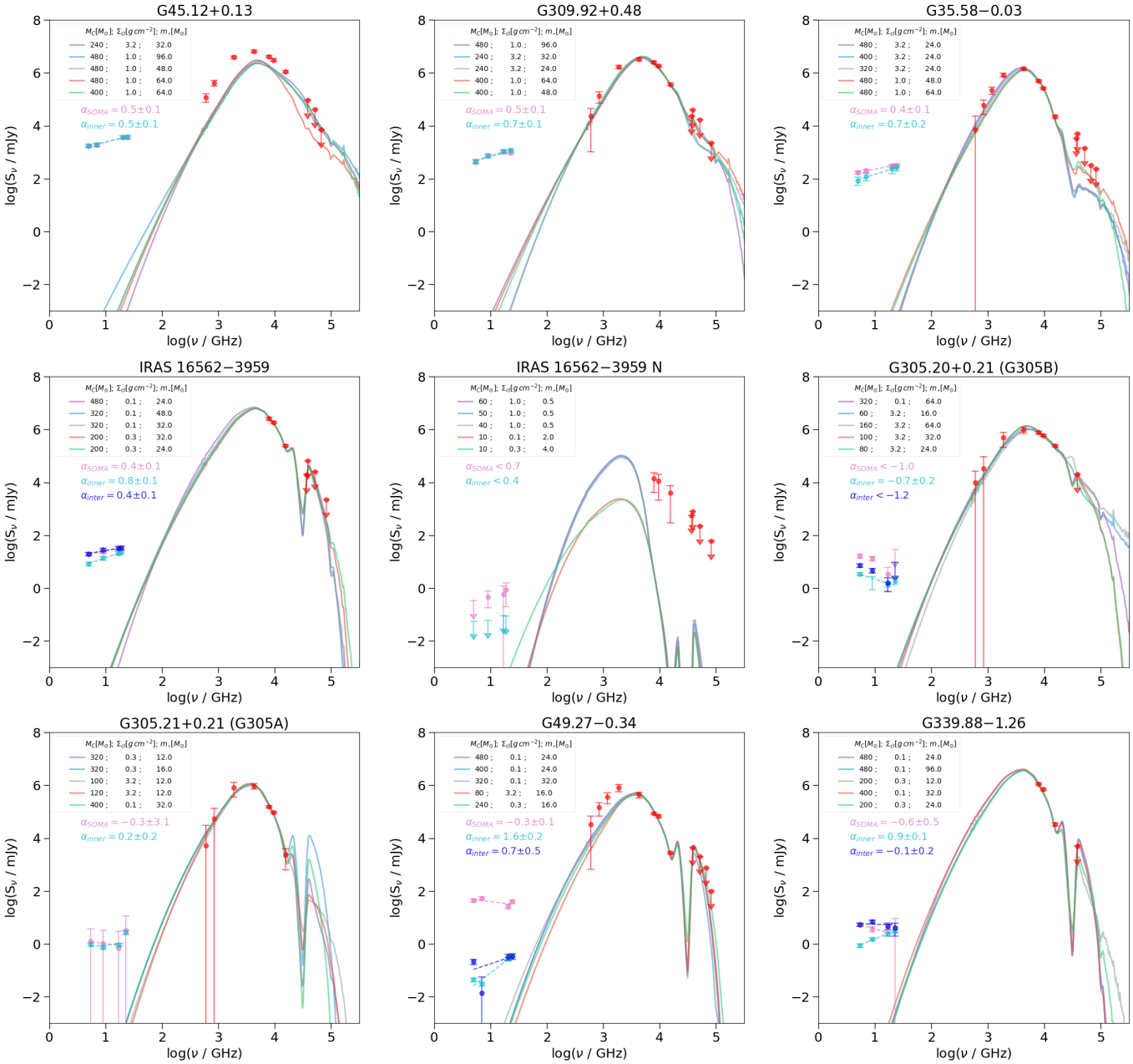

Figure 5. E-SEDs of SOMA protostars, consisting of radio and IR SEDs. Red circles show IR data for the SOMA apertures as measured by SOMA II. The other colored circles correspond to the centimeter flux density as a function of the frequency at each scale (magenta: SOMA; blue: intermediate; cyan: inner). Error bars are explained in Section 3.2. The solid lines show the five best fits (see legend) to the IR data SED from the Y. Zhang & J. C. Tan (2018) models as fit by SOMA IV (see the appendix in SOMA IV), and the dashed lines are the best fit of the radio data using a power law of the form $S_\nu \propto \nu^\alpha$.

$S_\nu \propto \nu^\alpha$, where α is the spectral index at the various scales: "SOMA"; "intermediate"; and "inner," as described in Section 3. The spectral index was calculated using the flux density at the central frequencies from the images, so α is calculated over a wide frequency range (>20 GHz). The uncertainty in the spectral index was calculated with a Monte Carlo simulation that bootstrapped the flux density uncertainties. We estimated an upper limit in the spectral index for nondetections at higher frequencies using a value of S_ν of 3σ.

It is important to mention that at higher frequencies the free–free emission is likely contaminated by dust emission (see C. L. Brogan et al. 2016); therefore, adding some additional systematic uncertainty to the measurement of the free–free fluxes.

4. Analysis and Discussion

The main goal of this paper is to analyze the morphology, multiplicity, and the estimated spectral indices of the sources of the SOMA II sample to better understand the nature of the sources using radio observations at different frequencies. Our sample consists of regions located at distances greater than 1 kpc, with some exhibiting low radio flux densities (<3 mJy), such as G305.20+0.21 (G305B), G305.21+0.21 (G305A), G49.27-0.34, and G339.88-1.26. In contrast to SOMA Radio I, seven of the eight sources analyzed showed relatively low radio flux densities.

With the available data, we aim to assess the nature of the sources based on their morphology and spectral index. For

sources that have been previously analyzed, we refer to past studies that have characterized their nature and compare our results, specifically in terms of morphology and spectral index (see Section 3.1). This comparison allows us to refine our understanding of the radio emission mechanisms associated with each source.

4.1. Multiplicity and New Detections

Most of the sources analyzed in this paper present a high level of multiplicity, except for G305A, which only has one detection within the SOMA scale. Furthermore, no source has been detected in IRAS 16562 N at the sensitivity level ($\sim$21–28 μJy) of the analyzed ATCA data.

Across our nine target regions, we detected a total of 37 sources. See Section 3.1 for individual analysis of each source. About 38% of the sources are new detections; hence, in Section 3.1, we made the notation of two types of new detections: (A) sources that have been previously observed and detected at different wavelengths, but not at radio frequencies; and (B) sources that have never been detected at any wavelength. This type of new detection could be regions that have been observed at radio but remained undetected due to limitations of sensitivity or possible variable sources. Detections of regions in which we present the first radio observations also fall in this category.

Of the 37 sources, we report 13 new detections (9 in G35.58-0.03, 1 in IRAS 16562-3959, and 3 in G305B or G305.20+0.2) classified as Type B detections, which, to the best of our knowledge, have never been detected at any wavelength.

To make sure we are not missing any UC HII regions, we estimate the physical properties from the 5 GHz sensitivity limit (rms) using Equation (1) and (3) from S. Kurtz et al. (1994) and equation A.2.3 from N. Panagia & C. M. Walmsley (1978). These equations assume spherical symmetry and optically thin emission from a uniform-density plasma with $T_e = 10^4$ K. The results are listed in Table 9, where column (1) is the region name, column (2) is the logarithm of the Lyman continuum flux ($\log N'_{\rm Ly}$) required for ionization. With the $\log N'_{\rm Ly}$ and the results from Table II in N. Panagia (1973), we estimate the spectral type of the ionizing star (listed in column (3)), further assuming that a single ZAMS star is photoionizing the nebula and producing the Lyman continuum flux. The distances used for these calculations are listed in Table 1. Column (4) is the estimated mass of the spectral type of the ionizing star from M. J. Pecaut & E. E. Mamajek (2013).

The results from Table 9 give us an estimation of the lowest-mass ZAMS star that we can detect with our current observations. This serves as a completeness parameter on the multiplicity at the different regions, especially for region IRAS 16562-3959 N, where we do not report any detections, and in this case, the completeness level goes down to around 5.4 $M_\odot$.

4.2. Nature of the Sources

By using previous studies on these sources, as well as results from our radio observations, we have assessed the nature of each individual source (see Section 3.1). From a sample point of view of the SOMA II sources, out of the 37 detections, it is important to mention that three of them are well-defined radio jets, given their morphology and the estimated spectral index. For example, IRAS 16562-3959 and G339.88-1.26 are both very well previously studied ionized jets. Both have a central source that exhibits a jetlike morphology and a spectral index in the range for typical ionized jets associated with YSOs (S. P. Reynolds 1986; G. Anglada et al. 1998; K. E. I. Tanaka et al. 2016), along with two additional sources classified as lobes that display nonthermal emission due to the synchrotron radiation. For G49.27-0.34 CM2A, we report a spectral index in the typical range of ionized jets and two additional sources relatively close to the driving jet (CM2B at 0.″7 and CM2C at 1.″2), but both companions exhibit thermal emission.

We also propose a radio jet scenario for sources G35.58–0.03, G305.21+0.21 (G305A), and G305.20+0.21 (G305B), based on the calculated spectral index, observed extended morphology, association with extended molecular outflows, and, in some cases, evidence of knots from a nonthermal jet in the direction of the elongation. However, this classification remains less certain compared to other radio jets in the sample, and additional observations are needed to fully resolve and confirm the presence of the proposed nonthermal jets.

Additionally, we have three UC H II regions (G45.12+0.13 S14, G35.58-0.03 31, and IRAS 16562-3959 2), following the suggestion of previous authors and the morphology of our detections and the reported spectral indices. The remaining sources are point sources, being companion sources from the central detection or sources of an unknown nature, that could be of extragalactic nature or lower-mass YSOs. Most of them display a flat or negative spectral index, suggesting nonthermal emission. Table 10 summarizes all the sources reported in this paper, along with their suggested nature. Column (1) lists the region, column (2) the corresponding source name, and column (3) the suggested nature of the source.

In terms of multiplicity, we find results similar to SOMA Radio I, where the analyzed regions exhibit high multiplicity, with multiple sources detected within the SOMA scale. In SOMA Radio I, seven out of eight regions showed at least two detections. In our sample, seven out of nine regions also show more than one detection, with G305.21+0.21 (G305A) having a single detection and IRAS 16562-3959 N showing no detections, likely due to our sensitivity limit.

In SOMA Radio I, we reported different evolutionary stages and the nature of the sample, which included radio jets, H II

Table 9
Parameters from Radio Continuum at the Sensitivity Limit at 5 GHz

Region	$\log N'_{\rm Ly}$[a]	Sp[b]	$M_\odot$[c]
G45.12+0.13	45.34	B1	11.8
G309.92+0.48	46.03	B0.5	14.8
G35.58-0.03	45.49	B1	11.8
IRAS 16562-3959	43.38	B3	5.4
IRAS 16562-3959 N	43.40	B3	5.4
G305.20+0.21	44.98	B1	11.8
G305.20+0.21 A	44.96	B1	11.8
G49.27-0.34	44.07	B3	5.4
G339.88-1.26	44.01	B3	5.4

Notes.
[a] Values calculated using equations from S. Kurtz et al. (1994), N. Panagia & C. M. Walmsley (1978).
[b] Spectral type estimation made from table II in N. Panagia (1973).
[c] The estimate of the mass was taken from M. J. Pecaut & E. E. Mamajek (2013)

Table 10
Summary of the Nature of the Sources Reported in the SOMA II Sample

Region	Source	Nature
G45.12+0.13	S14	UC H II Region
G45.12+0.13	S20	Extragalactic
G309.92+0.48	ATCA1	Optically Thick emitter
G309.92+0.48	ATCA2	Undetermined
G35.58-0.03	30A	Undetermined
G35.58-0.03	30B	Jet Knot (Candidate)
G35.58-0.03	30C	Jet Knot (Candidate)
G35.58-0.03	30D	Jet Knot (Candidate)
G35.58-0.03	30E	Jet Knot (Candidate)
G35.58-0.03	30F	Jet Knot (Candidate)
G35.58-0.03	30G	Jet Knot (Candidate)
G35.58-0.03	30H	Jet Knot (Candidate)
G35.58-0.03	30J	Jet Knot (Candidate)
G35.58-0.03	30K	Jet Knot (Candidate)
G35.58-0.03	30N	Unresolved Jet Candidate
G35.58-0.03	30S	Unresolved Jet Candidate
G35.58-0.03	31	UC HII Region
IRAS 16562-3959	C	Ionized Radio Jet
IRAS 16562-3959	I-E	Nonthermal Lobe
IRAS 16562-3959	I-W	Nonthermal Lobe
IRAS 16562-3959	1	Extragalactic
IRAS 16562-3959	2	HC HII Region
IRAS 16562-3959	3	Low-mass YSO
IRAS 16562-3959	4	Undetermined
G305.21+0.21 (G305A)	ATCA-1	Jet Candidate
G305.20+0.21 (G305B)	ATCA-1	Jet Candidate
G305.20+0.21 (G305B)	ATCA-2	Jet Knot (Candidate)
G305.20+0.21 (G305B)	ATCA-3	Part of the H II Region
G305.20+0.21 (G305B)	ATCA-4	Jet Knot (Candidate)
G49.27-0.34	CM1	B0V Ionizing Star
G49.27-0.34	CM2A	Jet Candidate
G49.27-0.34	CM2B	Jet Knot (Candidate)
G49.27-0.34	CM2C	Jet Knot (Candidate)
G49.27-0.34	CM3	Undetermined
G339.88-1.26	C	Ionized Radio Jet
G339.88-1.26	NE	Nonthermal Lobe
G339.88-1.26	SW	Nonthermal Lobe

regions, and variable stars. Four of the seven sources in that initial sample exhibited characteristics consistent with radio jets, such as elongation in the same direction as the associated molecular outflow, with a central ionized jet and knots in aligned detections. In the sample presented in this paper, we observe a similar distribution: six of the nine regions show evidence of hosting a radio jet on the SOMA scale. Of these six, three (IRAS 16562-3959, G49.27-0.34, G339.88-1.26) display well-defined jets with knots, while the remaining two (G305A: G305.21+0.21, G305B: G305.20+0.21 and G35.58-0.03) are proposed as jet candidates based on characteristics discussed in detail in Section 3, including spectral index, morphology, and multiplicity. Additionally, source G45.12 +0.13 has been previously reported to be associated with a UC HII region, which is consistent with our assessment from Figure 6 (see below). Furthermore, this source shows ionized emission at the lowest frequency (L band) that resembles an hour-glass morphology similar to the very massive protostar G45.47+0.05, which is also associated with a UC H II region that is driving a powerful photoionized outflow and a jet candidate (Y. Zhang et al. 2019b).

4.3. The Radio—Bolometric Luminosity Relation

Here, we expand on the analysis of the SOMA sample from the results presented in SOMA Radio I, which presented results for an initial sample of eight massive protostars. We add the nine protostars selected from the seven high-luminosity regions analyzed in this paper.

Similar to Figure 3 in SOMA Radio I, in Figure 6, we present radio luminosity at 5 GHz from the inner (left panel) and SOMA (right panel) scales versus bolometric luminosity. Note, when necessary, radio fluxes at $\nu = 5$ GHz have been estimated by scaling from adjacent frequencies using the derived spectral index. For the bolometric luminosity of SOMA sources (detections from SOMA I and II samples are squares and circles, respectively), we report the average of the "good" models from Table C1 of SOMA V, and the error bar corresponds to the dispersion of these good models. We also show data for lower-mass YSOs associated with ionized jets from G. Anglada (1995; small yellow dots). We scaled their fluxes from 3.6 cm, using a factor of 0.74, assuming that these sources have a spectral index $\alpha = 0.6$, which is the expected value of ionized jets. A power-law fit to these data of $(S_\nu d^2/[\mathrm{mJy\ \ kpc^2}]) = 8 \times 10^{-3}(L_{\rm bol}/L_\odot)^{0.6}$ is shown with a dashed line. UC/HC H II regions from S. Kurtz et al. (1994) are represented with $\times$ symbols. Note, the bolometric luminosities of the low-mass YSOs and the UC/HC H II regions are not measured in exactly the same way as the SED-fitting method of the SOMA sources, for which we are reporting intrinsic bolometric luminosities of the fitted SED models. A plot showing the results based on isotropic bolometric luminosities is presented in Appendix A.

We examine several theoretical models for the radio luminosity of massive protostars and show these in Figure 6. The black dotted line is the radio emission expected from an optically thin H II region, given the Lyman continuum luminosity of a single ZAMS star at a given bolometric luminosity (R. I. Thompson 1984). The light blue lines correspond to the expected radio emission that arises from photoionization from a massive protostar, forming via TCA, as predicted by the TTZ16 model, also for optically thin conditions at 5 GHz. These models have an initial core mass of $M_c = 60\,M_\odot$ and the three cases correspond to clump environment mass surface densities of $\Sigma_{\rm cl} = 0.316$, 1 and 3.16 g cm^{-2}. The lower mass surface densities correspond to lower accretion rates, for which protostellar contraction toward the ZAMS occurs sooner, i.e., at lower masses and lower values of $L_{\rm bol}$. Note, these models do not include any contribution from shock ionization.

A model for estimating the radio emission from free–free emission from ionized gas produced by collisional ionization in shocks has been developed for a massive protostar-forming from a $60\,M_\odot$ core in a 1 g cm^{-2} clump environment by E. C. Gardiner et al. (2024). This radio emission is also shown in Figure 6 with dark blue lines. We note that the contribution from shock ionization is quite spatially extended, with the emission from a 25,000 au radius aperture (more closely matching the SOMA scale) being about a factor of 10 higher than that from a 1000 au aperture (more closely matching the inner scale).

Comparing the distribution of SOMA Radio sources with the models, we note the following points. The SOMA Radio II sample, mostly being protostars of relatively high luminosity,

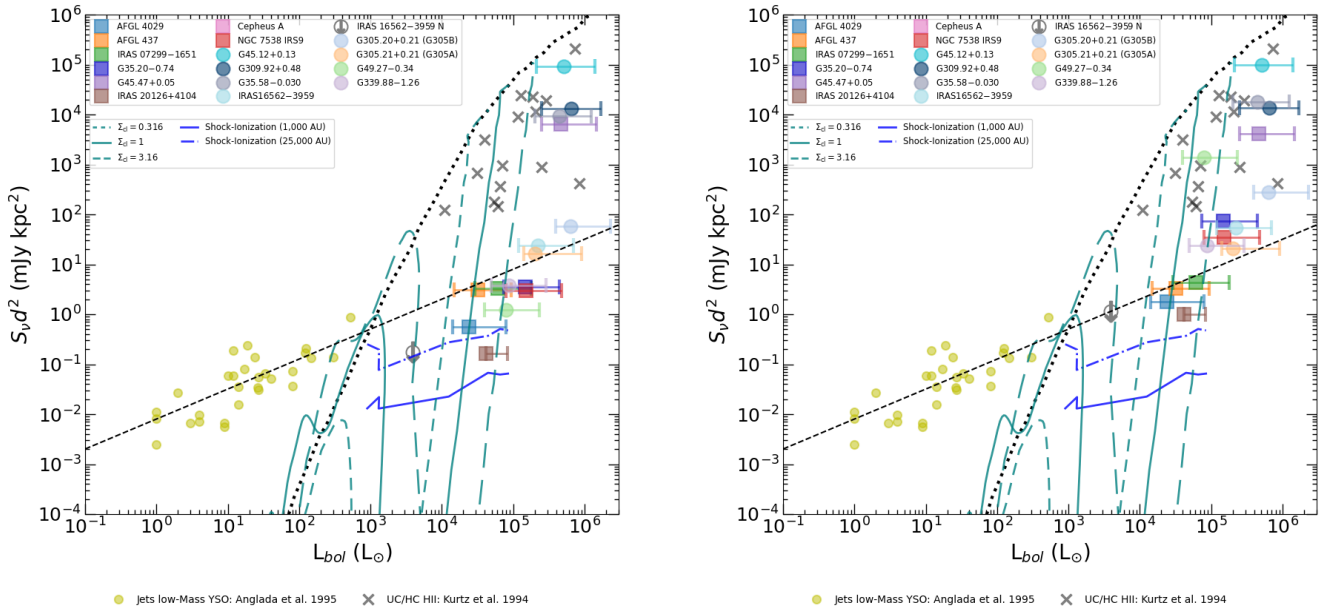

Figure 6. Radio luminosity at 5 GHz for the inner scale (left) and for the SOMA scale (right) as a function of the bolometric luminosity for 15 SOMA sources from SOMA Radio I (squares) and II (circles; see legend). In each panel, we also show lower-mass YSOs from G. Anglada (1995; small yellow circles). The dashed line shows a power-law fit to these lower-mass YSOs (G. Anglada et al. 2015): $(S_\nu d^2/[\mathrm{mJy\ \ kpc^2}]) = 8 \times 10^{-3}(L_{\rm bol}/L_\odot)^{0.6}$. The × symbols are HC and UC H II regions from S. Kurtz et al. (1994). The black dotted line shows the radio emission expected from optically thin H II regions powered by ZAMS stars (R. I. Thompson 1984). The light blue lines show models for H II regions powered by TCA model protostars (K. E. I. Tanaka et al. 2016; with $M_c = 60\,M_\odot$ and $\Sigma_{\rm cl} =$ 0.316, 1, and 3.16 g cm^{-2}, as labeled). Note that these models, which do account for radiative transfer effects of the free–free emission, assume all of the ionizing photons are reprocessed by the H II region, i.e., with zero escape fraction. The dark blue lines show radio emission from shock ionization in simulations of a fiducial TCA protostar, i.e., forming from a 60 $M_\odot$ core in a 1 g cm^{-2} clump environment (E. C. Gardiner et al. 2024), with the solid and dotted–dashed lines showing emission from within 1000 and 25,000 au of the protostar, respectively.

helps to better define the radio versus bolometric luminosity relation over the range from $L_{\rm bol} \sim 10^4$ to $10^6\,L_\odot$, which is a regime where it is rising rapidly. We find that the radio luminosity measured on the SOMA scale rises steeply by about four dex as bolometric luminosity increases by ∼1 dex from $\sim 10^{4.5} L_\odot$ to $\sim 10^{5.5}\,L_\odot$. Such a steep rise is consistent with basic expectations of TCA massive protostar models.

Nevertheless, overall, from the SOMA protostar sample, we see that sources have relatively faint radio luminosities compared to predictions of protostellar models. This suggests that the rise in ionizing luminosity may occur only at relatively higher protostellar masses and luminosities. Such a relatively late rise in ionizing luminosity could be due to higher protostellar accretion rates or reflect systematic errors in the current protostellar models and their HII region radio emission (e.g., assumption that all stellar EUV photons contribute to ionization/neglect of dust absorption). In addition, we caution that, at least on the SOMA scale, there is the possibility that we are missing radio flux due to interferometric filtering. A comparison with additional sets of theoretical models based on optically thin radio emission from the ionizing photon output of the TCA protostellar evolution models of Y. Zhang & J. C. Tan (2018) is shown in Appendix B.

The differences between the results shown in the two plots of Figure 6 (as well as Figures A1, B1, and B2), particularly for the sources we classified as having jetlike morphologies (G305.20+0.21, G305.21+0.21, IRAS 16562-3959, G339.88 −1.26, and G49.27−0.34), arise from the different scales used to determine the radio luminosity (Ü. Kavak et al. 2021). As noted by W. O. Obonyo et al. (2024), when measuring well-resolved cores of radio jets, the sources tend to align with the fit of lower-mass YSOs associated with ionized jets (dashed line in Figure 6). For our inner scale (left plot), in most cases we were able to resolve the driving source of the radio jet and therefore all of our jet candidates fall in the low-mass fit within uncertainties, except for source G49.27-0.34.

The SOMA scale (right plot) takes all the emission in the region into account, adding contaminating emission from the jet knots and other sources within this region, further enhancing the radio luminosity. The artificial emission added by other sources and the different spatial scales, when compared to the inner scale, make the SOMA scale not as reliable to study the nature of the sources as the inner scale, but the SOMA scale still holds importance since it allows for direct comparison with theoretical models with bigger scales that take jet knots and other multiple stellar sources in protoclusters into account.

We note that the HC/UC H II region sample of S. Kurtz et al. (1994) does include sources with higher radio luminosities, potentially indicating a systematic change arising from source evolution from the protostellar phase or else reflecting biases in sample selection from a single intrinsic protostellar population that has inherent large variation in radio luminosity.

We see that the shock ionization model of E. C. Gardiner et al. (2024), which falls below the extrapolated lower-mass YSO relation, is consistent with the fainter end of the SOMA sample. Extending the comparison of the models with SOMA data on intermediate-mass protostars is a major goal of the SOMA Radio III paper (in preparation).

5. Summary and Conclusions

We have presented results from radio continuum VLA and ATCA follow-up observations of massive protostars of the SOMA II sample following the framework developed

in SOMA Radio I. These radio observations help to give a precise localization of the protostar, allow a search for multiplicity, and trace the presence of ionized gas, which helps trace outflow morphology, especially via orientation of radio jet axes, and is expected to be a useful evolutionary indicator of massive protostars, especially as they approach the ZAMS when the contribution from photoionization is predicted to increase dramatically.

A summary of the main findings is as follows. We have detected and analyzed emission from eight out of the nine massive protostars (from seven primary regions), with the nondetection being related to IRAS 16562-3959 N, which is an intermediate-mass protostar that is a secondary source in this region. Similar to the SOMA Radio I regions, we have found a high level of "multiplicity" with 37 detections in the seven regions. However, we caution that many of these sources are likely to be ionized gas jet knots, rather than independent stellar sources. Higher sensitivity observations are needed to better probe the presence of lower-mass YSOs that may be in the vicinity.

Given that the seven primary protostars of the SOMA II sample were selected as being relatively high bolometric luminosity protostars, these data help to better define the radio–bolometric luminosity relation in this regime, i.e., from $\sim 10^4$ to $10^6 L_\odot$. We find that the radio luminosity, i.e., at 5 GHz, rises steeply by about 5 dex as bolometric luminosity increases by 1 dex. However, the caveat of the possibility of missing flux from extended ionized gas features needs to be kept in mind.

Many of our fainter radio sources have radio luminosities that are consistent with a simple power law extrapolation from a lower-mass YSO sample (G. Anglada 1995). However, this radio flux is about 10 times higher than a theoretical model of radio emission from shock ionization of a fiducial TCA massive protostar (E. C. Gardiner et al. 2024). Nevertheless, shock ionization appears to be the most likely explanation for many of these sources, especially given the morphology of extended jet knots, while a contribution from photoionization, especially at the inner scale, cannot be excluded. However, in the high-radio-luminosity regime, photoionization is expected to be dominant. Overall, these data are important for constraining theoretical models of massive protostar ionization and how this links to protostellar structure and evolutionary state.

Acknowledgments

We thank the anonymous referee for helpful comments that improved this manuscript. We acknowledge Dr. Simon Purser and Dr. Andres Guzmán for providing the ATCA images for sources G339.88–1.26 and IRAS 16562–3959 presented in A. E. Guzmán et al. (2016) and B. Partridge et al. (2016), respectively. F.S.M. acknowledges support from the NRAO NINE (National and International Nontraditional Exchange) program. V.R. acknowledges support from NSF grant AST–2206437 to the Space Science Inst. J.C.T. acknowledges support from NSF grant AST–2206437 and ERC Advanced Grant 788829 (MSTAR). R.F. acknowledges support from the grants PID2023-146295NB-I00 and from the Severo Ochoa grant CEX2021-001131-S funded by MCIN/AEI/ 10.13039/501100011033 and by "European Union NextGenerationEU/PRTR." The National Radio Astronomy Observatory and Green Bank Observatory are facilities of the U.S. National Science Foundation operated under cooperative agreement by Associated Universities, Inc.

Facilities: VLA, ATCA.

Software: CASA (J. P. McMullin et al. 2007), Astropy (Astropy Collaboration et al. 2013, 2018), APLpy (T. Robitaille et al. 2012; T. Robitaille 2019).

Appendix A
Radio Luminosity Versus Isotropic Bolometric Luminosity

Figure A1 shows a similar plot to Figure 6, but in this case, we used the average of the good models of the isotropic bolometric luminosity (Table C.1 of SOMA V). Everything else is the same as Figure 6.

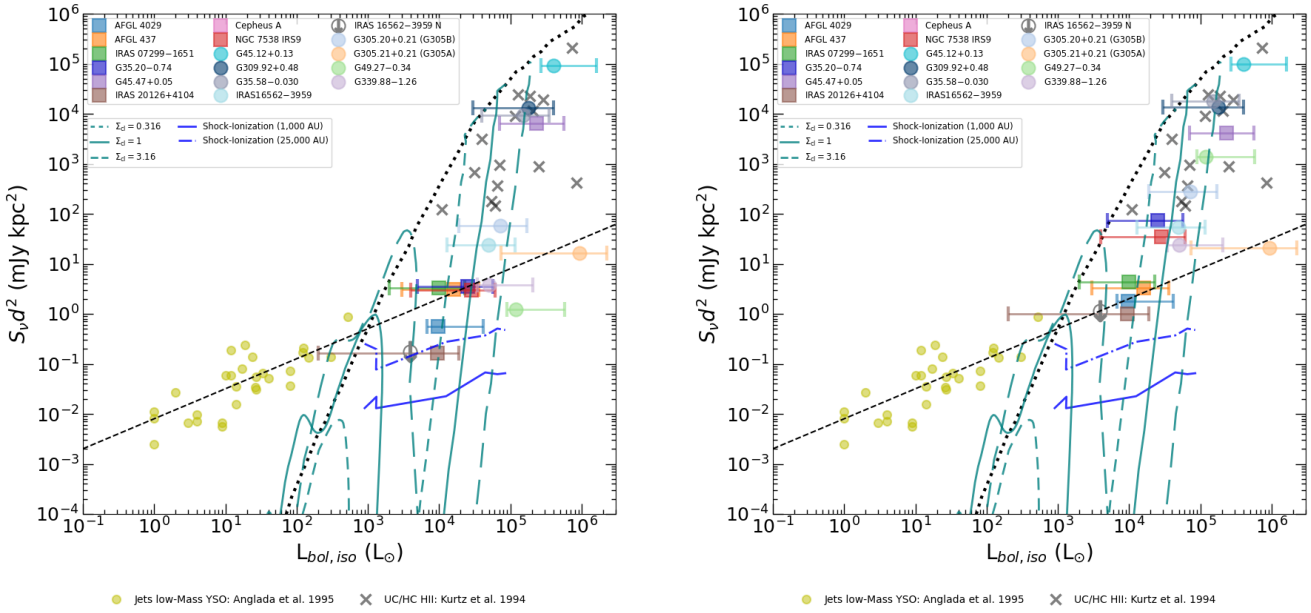

Figure A1. As Figure 6, but now plotting $L_{\rm bol,iso}$ for the SOMA sources (left: inner scale, right: SOMA scale).

Appendix B
Evolutionary Tracks from Radio Luminosities

Figure B1 makes a comparison of the SOMA Radio data at the inner (top) and SOMA (bottom) scale, with the full set of protostellar evolutionary tracks from Y. Zhang & J. C. Tan (2018), i.e., with $M_c =$ 10, 30, 60, 120, 240 and 480 $M_\odot$ with $\Sigma_{cl} =$ 0.316 g cm^{-2} (left), 1 g cm^{-2} (center) and 3.16 g cm^{-2} (right). In these models, the radio luminosities are not set from radiation transfer like the tracks from (K. E. I. Tanaka et al. 2016), but instead assume a simple spherical H II region. Meanwhile, Figure B2 shows the same information but with the average of the good models of the isotropic bolometric luminosity (Table C.1 of SOMA V).

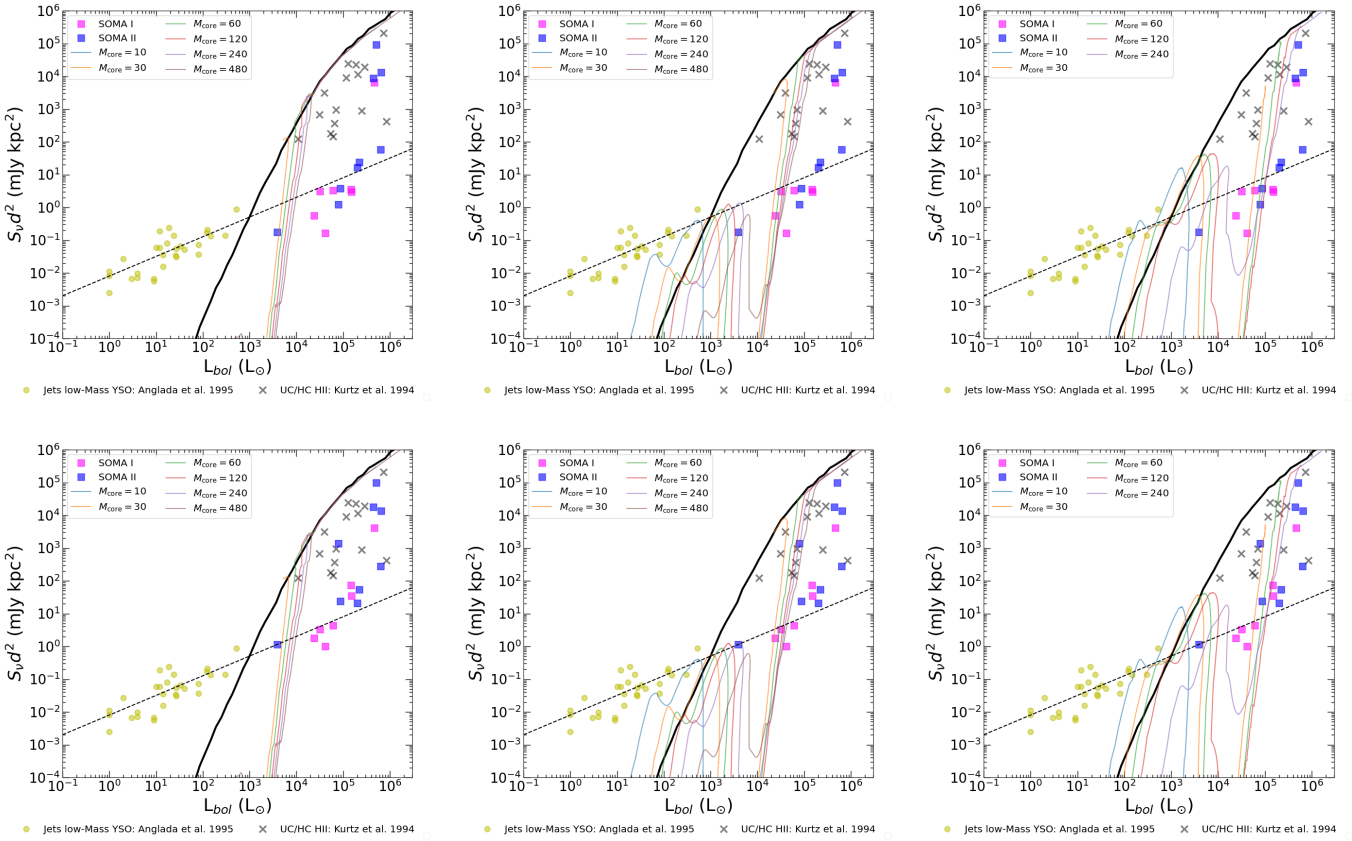

Figure B1. As Figure 6, but now showing protostellar evolutionary tracks from Y. Zhang & J. C. Tan (2018), under the assumption of optically thin radio emission. These models are for $M_c =$ 10, 30, 60, 120, 240, and 480 $M_\odot$ with $\Sigma_{cl} =$ 0.316 g cm^{-2} (left), 1 g cm^{-2} (center), and 3.16 g cm^{-2} (right). The top plots are with the radio luminosity at the inner scale, and the bottom plots are with the radio luminosity at the SOMA scale.

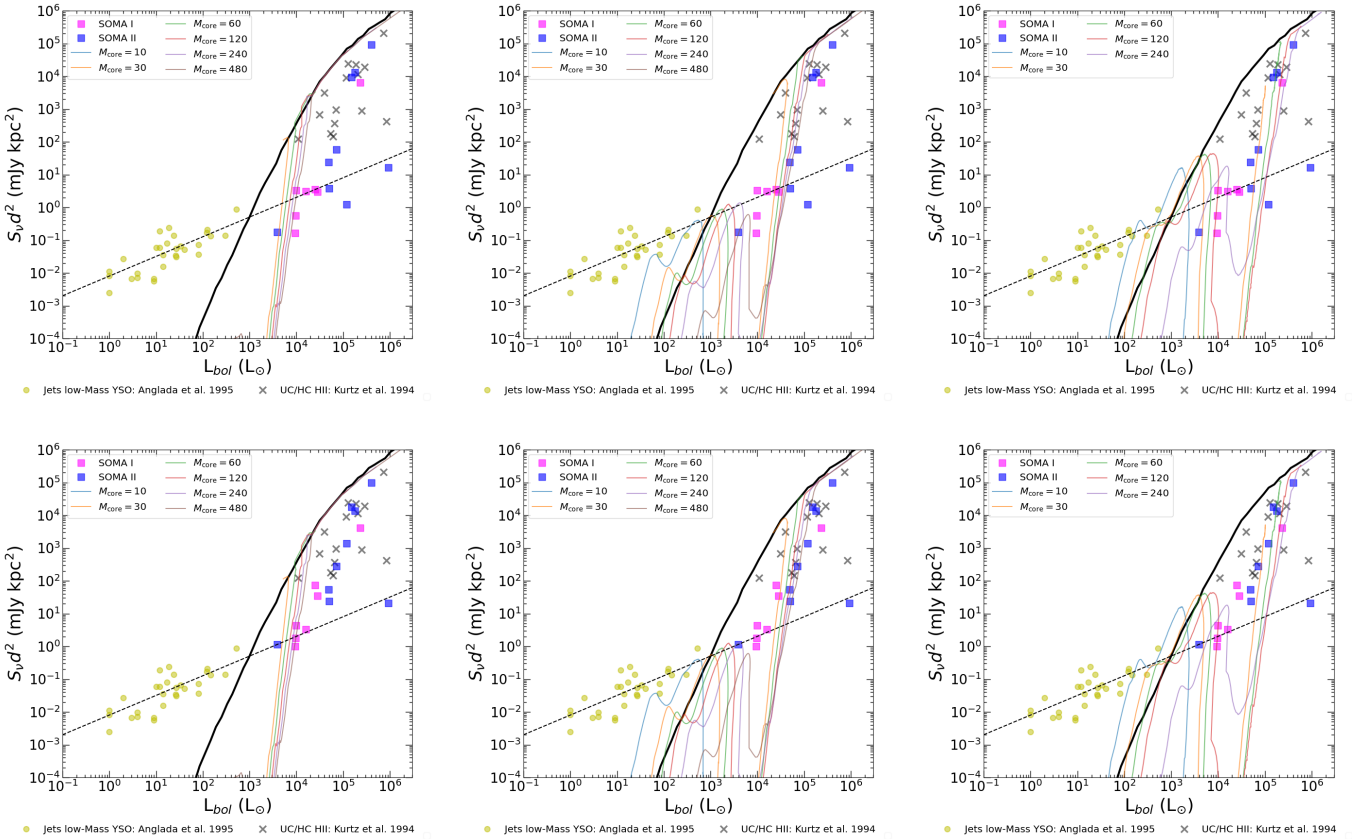

Figure B2. As Figure B1, but now with the isotropic bolometric luminosity. The top plots are with the radio luminosity at the inner scale, and the bottom plots are with the radio luminosity at the SOMA scale.

ORCID iDs

Francisco Sequeira-Murillo https://orcid.org/0000-0001-8169-1437
Viviana Rosero https://orcid.org/0000-0001-8596-1756
Joshua Marvil https://orcid.org/0000-0003-1111-8066
Jonathan C. Tan https://orcid.org/0000-0002-3389-9142
Ruben Fedriani https://orcid.org/0000-0003-4040-4934
Yichen Zhang https://orcid.org/0000-0001-7511-0034
Azia Robinson https://orcid.org/0009-0007-4080-9807
Prasanta Gorai https://orcid.org/0000-0003-1602-6849
Kei E. I. Tanaka https://orcid.org/0000-0002-6907-0926
James M. De Buizer https://orcid.org/0000-0001-7378-4430
Maria T. Beltrán https://orcid.org/0000-0003-3315-5626
Ryan D. Boyden https://orcid.org/0000-0001-9857-1853

References

Anglada, G. 1995, in RMxAA, ed. S. Lizano & J. M. Torrelles, 67
Anglada, G., Rodríguez, L. F., & Carrasco-Gonzalez, C. 2015, in Proceedings of Advancing Astrophysics with the Square Kilometre Array (AASKA14) (PoS), 121
Anglada, G., Villuendas, E., Estalella, R., et al. 1998, AJ, 116, 2953
Argon, A. L., Reid, M. J., & Menten, K. M. 2000, ApJS, 129, 159
Astropy Collaboration, Price-Whelan, A. M., Sipőcz, B. M., et al. 2018, AJ, 156, 123
Astropy Collaboration, Robitaille, T. P., Tollerud, E. J., et al. 2013, A&A, 558, A33
Azatyan, N., Nikoghosyan, E., Harutyunian, H., Baghdasaryan, D., & Andreasyan, D. 2022, PASA, 39, e024
Bonnell, I. A., Bate, M. R., Clarke, C. J., & Pringle, J. E. 2001, MNRAS, 323, 785
Bonnell, I. A., Bate, M. R., & Zinnecker, H. 1998, MNRAS, 298, 93
Briggs, D. S. 1995, PhD Thesis, New Mexico Institute of Mining and Technology
Brogan, C. L., Hunter, T. R., Cyganowski, C. J., et al. 2016, ApJ, 832, 187
Carey, S. J., Noriega-Crespo, A., Mizuno, D. R., et al. 2009, PASP, 121, 76
Caswell, J. L. 1997, MNRAS, 289, 203
Caswell, J. L., Vaile, R. A., Ellingsen, S. P., Whiteoak, J. B., & Norris, R. P. 1995, MNRAS, 272, 96
Cyganowski, C. J., Brogan, C. L., Hunter, T. R., & Churchwell, E. 2009, ApJ, 702, 1615
Cyganowski, C. J., Brogan, C. L., Hunter, T. R., & Churchwell, E. 2011, ApJ, 743, 56
De Buizer, J. M., Liu, M., Tan, J. C., et al. 2017, ApJ, 843, 33
De Buizer, J. M., Piña, R. K., & Telesco, C. M. 2000, ApJS, 130, 437
De Buizer, J. M., Walsh, A. J., Piña, R. K., Phillips, C. J., & Telesco, C. M. 2002, ApJ, 564, 327
Ellingsen, S. P., Norris, R. P., & McCulloch, P. M. 1996, MNRAS, 279, 101
Fedriani, R., Tan, J. C., Telkamp, Z., et al. 2023, ApJ, 942, 7
Gardiner, E. C., Tan, J. C., Staff, J. E., et al. 2024, ApJ, 967, 145
Ginsburg, A., Darling, J., Battersby, C., Zeiger, B., & Bally, J. 2011, ApJ, 736, 149
Grudić, M. Y., Guszejnov, D., Offner, S. S. R., et al. 2022, MNRAS, 512, 216
Guzmán, A. E., Garay, G., & Brooks, K. J. 2010, ApJ, 725, 734
Guzmán, A. E., Garay, G., Brooks, K. J., Rathborne, J., & Güsten, R. 2011, ApJ, 736, 150
Guzmán, A. E., Garay, G., Rodríguez, L. F., et al. 2014, ApJ, 796, 117
Guzmán, A. E., Garay, G., Rodríguez, L. F., et al. 2016, ApJ, 826, 208
Hill, T., Burton, M. G., Minier, V., et al. 2005, MNRAS, 363, 405
Hunter, T. R., Phillips, T. G., & Menten, K. M. 1997, ApJ, 478, 283
Kalcheva, I. E., Hoare, M. G., Urquhart, J. S., et al. 2018, A&A, 615, A103
Kavak, Ü., Sánchez-Monge, Á., López-Sepulcre, A., et al. 2021, A&A, 645, A29
Krishnan, V., Ellingsen, S. P., Reid, M. J., et al. 2015, ApJ, 805, 129

Krishnan, V., Ellingsen, S. P., Reid, M. J., et al. 2017, MNRAS, 465, 1095
Kurtz, S., Churchwell, E., & Wood, D. O. S. 1994, ApJS, 91, 659
Liu, M., Tan, J. C., De Buizer, J. M., et al. 2019, ApJ, 874, 16
Liu, M., Tan, J. C., De Buizer, J. M., et al. 2020, ApJ, 904, 75
McKee, C. F., & Tan, J. C. 2003, ApJ, 585, 850
McMullin, J. P., Waters, B., Schiebel, D., Young, W., & Golap, K. 2007, in ASP Conf. Ser. 376, Astronomical Data Analysis Software and Systems XVI, ed. R. A. Shaw, F. Hill, & D. J. Bell (ASP), 127
Mehringer, D. M. 1994, ApJS, 91, 713
Montes, V. A., Hofner, P., Oskinova, L. M., & Linz, H. 2020, ApJ, 888, 118
Murphy, T., Cohen, M., Ekers, R. D., et al. 2010, MNRAS, 405, 1560
Norris, R. P., Whiteoak, J. B., Caswell, J. L., Wieringa, M. H., & Gough, R. G. 1993, ApJ, 412, 222
Obonyo, W. O., Hoare, M. G., Lumsden, S. L., et al. 2024, MNRAS, 533, 3862
Panagia, N. 1973, AJ, 78, 929
Panagia, N., & Walmsley, C. M. 1978, A&A, 70, 411
Partridge, B., López-Caniego, M., Perley, R. A., et al. 2016, ApJ, 821, 61
Patel, A. L., Urquhart, J. S., Yang, A. Y., et al. 2025, MNRAS, 538, 2267
Pecaut, M. J., & Mamajek, E. E. 2013, ApJS, 208, 9
Phillips, C. J., Norris, R. P., Ellingsen, S. P., & McCulloch, P. M. 1998, MNRAS, 300, 1131
Purser, S. J. D., Lumsden, S. L., Hoare, M. G., & Kurtz, S. 2021, MNRAS, 504, 338
Purser, S. J. D., Lumsden, S. L., Hoare, M. G., et al. 2016, MNRAS, 460, 1039
Reynolds, S. P. 1986, ApJ, 304, 713
Robitaille, T. 2019, APLpy v2.0: The Astronomical Plotting Library in Python, Zenodo, doi: 10.5281/zenodo.2567476
Robitaille, T., Bressert, E., et al., 2012 APLpy: Astronomical Plotting Library in Python, Astrophysics Source Code, ascl:1208.017
Rosero, V., Hofner, P., Claussen, M., et al. 2016, ApJS, 227, 25
Rosero, V., Hofner, P., Kurtz, S., et al. 2019a, ApJ, 880, 99
Rosero, V., Tanaka, K. E. I., Tan, J. C., et al. 2019b, ApJ, 873, 20
Simon, R., Jackson, J. M., Clemens, D. P., Bania, T. M., & Heyer, M. H. 2001, ApJ, 551, 747
Tan, J. C., Beltrán, M. T., Caselli, P., et al. 2014, in Protostars and Planets VI, ed. H. Beuther, R.S. Klessen, C.P. Dullemond, & T. Henning (Univ. Arizona Press), 149
Tanaka, K. E. I., Tan, J. C., & Zhang, Y. 2016, ApJ, 818, 52
Telkamp, Z., Fedriani, R., Tan, J. C., et al. 2025, ApJ, 986, 15
Thompson, R. I. 1984, ApJ, 283, 165
Towner, A. P. M., Brogan, C. L., Hunter, T. R., et al. 2017, ApJS, 230, 22
Vig, S., Ghosh, S. K., Kulkarni, V. K., Ojha, D. K., & Verma, R. P. 2006, ApJ, 637, 400
Walsh, A. J., & Burton, M. G. 2006, MNRAS, 365, 321
Walsh, A. J., Burton, M. G., Hyland, A. R., & Robinson, G. 1998, MNRAS, 301, 640
Walsh, A. J., Burton, M. G., Hyland, A. R., & Robinson, G. 1999, MNRAS, 309, 905
Walsh, A. J., Chapman, J. F., Burton, M. G., Wardle, M., & Millar, T. J. 2007, MNRAS, 380, 1703
Wang, P., Li, Z.-Y., Abel, T., & Nakamura, F. 2010, ApJ, 709, 27
Watson, C., Araya, E., Sewilo, M., et al. 2003, ApJ, 587, 714
Wood, D. O. S., & Churchwell, E. 1989, ApJS, 69, 831
Yang, A. Y., Urquhart, J. S., Thompson, M. A., et al. 2021, A&A, 645, A110
Yang, A. Y., Urquhart, J. S., Wyrowski, F., et al. 2022, A&A, 658, A160
Zhang, C.-P., Wang, J.-J., Xu, J.-L., Wyrowski, F., & Menten, K. M. 2014, ApJ, 784, 107
Zhang, Y., & Tan, J. C. 2011, ApJ, 733, 55
Zhang, Y., & Tan, J. C. 2018, ApJ, 853, 18
Zhang, Y., Tan, J. C., & Hosokawa, T. 2014, ApJ, 788, 166
Zhang, Y., Tan, J. C., & McKee, C. F. 2013, ApJ, 766, 86
Zhang, Y., Tan, J. C., Sakai, N., et al. 2019a, ApJ, 873, 73
Zhang, Y., Tanaka, K. E. I., Rosero, V., et al. 2019b, ApJL, 886, L4